

Contents lists available at ScienceDirect

International Journal of Plasticity

journal homepage: www.elsevier.com/locate/ijplas





Quantifying dislocation drag at high strain rates with laser-induced Microprojectile impact

Qi Tang a, Mostafa Hassani a,b,*

- ^a Sibley School of Mechanical and Aerospace Engineering, Cornell University, Ithaca, NY 14853, USA
- ^b Department of Materials Science and Engineering, Cornell University, Ithaca, NY 14853, USA

ARTICLE INFO

Keywords: Constitutive modeling Microprojectile impact Spherical nanoindentation High Strain Rates Dislocation Drag

ABSTRACT

As deformation rate increases, the thermally activated dislocation glide gives way to a continuous glide of dislocations governed by their interactions with phonons. Understanding the dislocation-phonon drag regime is critical for designing metallic materials for extreme deformations rates. However, it has proven challenging to study empirically, partly due to the resource intensive nature of the experimental approaches targeting this regime. Here, we develop an impression-based experimental approach combining laser-induced microprojectile impact (Hassani et al., 2020a) and spherical nanoindentation to characterize the dislocation-phonon drag regime. We also develop a physically based constitutive framework that, when integrated with our experimental measurements, can quantify the dislocation-phonon drag regime. We isolate the effect of dislocation-phonon drag by leveraging the similar deformation geometries and length scales but different operative mechanisms during spherical nanoindentation and microprojectile impact. We discuss mechanistic contributions to the plastic work for microprojectile impacts in a range of impact velocities producing strain rates up to $10^9 \, {\rm s}^{-1}$. We also develop a deformation mechanism map focused on the transition from thermal activation to dislocation drag for a model FCC metal, copper.

1. Introduction

Mechanical behavior of metals at high deformation rates differs significantly from their response at low rates (Habib et al., 2021; Haridas et al., 2021; Liu et al., 2022; Meyers, 1994; Park et al., 2018; Wang et al., 2022; Zhang et al., 2020). At strain rates less than $\sim 10^3 \, \rm s^{-1}$, the flow stress shows relatively modest increments as the strain rate is increased by several orders of magnitude (Dubey et al., 2023; Lichtenfeld et al., 2006; Nie et al., 2020a). On the other hand, at strain rates higher than $10^3 - 10^4 \, \rm s^{-1}$, much higher strain rate sensitivities are observed; the flow stress increases significantly even with one order of magnitude increase in strain rate (Armstrong et al., 2009; Curtze and Kuokkala, 2010; Follansbee and Kocks, 1988; Ku et al., 2020; Li et al., 2019; B. B. Wang et al., 2019; Yuan et al., 2021). The transition from low to high strain rate sensitivities is associated with the change in the dominant deformation mechanism from thermally activated dislocation motion at lower rates to dislocation-phonon drag at higher rates (Blaschke et al., 2020; Kumar et al., 2015; Moćko et al., 2012; Sakino, 2006).

In the thermal activation regime, dislocations overcome the energy barriers imposed by discrete obstacles with the cooperation of the resolved shear stress and the thermally activated vibrations of atoms (INDENBOM and CHERNOV, 1992; Li and Huang, 2021;

E-mail address: hassani@cornell.edu (M. Hassani).

^{*} Corresponding author.

Zaretsky et al., 2023). As strain rate increases, shorter time is available for thermally activated jumps to assist dislocation glide. Consequently, the flow stress increases with increasing strain rate following a power law relation with relatively small exponents, $\sigma \propto \dot{\varepsilon}^m$ (m < 1) (Cao et al., 2019; El Ters and Shehadeh, 2019). Dislocations can only glide through obstacles continuously if the applied stress is high enough for them to overcome the energy barrier without relying on thermal activation (Blaschke et al., 2021; Regazzoni et al., 1987; Zhang et al., 2023). Continuous dislocation glide leads to an acceleration of dislocations to high velocities to accommodate an imposed high strain rate. Fast moving dislocations experience drag forces arising from their interaction with elementary lattice excitations such as phonons and electrons (ALSHITS, 1992; Olmsted et al., 2005; Rhee et al., 1998). At temperatures exceeding about one fifth of the Debye temperature phonon scattering and viscosity dominates the drag effect (Blaschke, 2019; Blaschke et al., 2020; Nadgornyi, 1988) and will be the primary focus in this work. In the dislocation-phonon regime, significantly higher strain rate sensitivities are observed with the power law exponent approaching unity, i.e., $\sigma \propto \dot{\varepsilon}$ (Meyers, 1994).

The linear proportionality between the drag force and the average dislocation velocity (Chandra et al., 2018; Kim and Kim, 2021; Yanilkin et al., 2014) has served as a focal point in a number of experimental techniques, as well as in atomistic simulations, to quantify the dislocation-phonon drag coefficient. Because the applied force or stress is typically a known factor, the objective in all these approaches is to determine the dislocation velocity or mobility (Greenman et al., 1967; Jassby and Vreeland, 1970). Direct imaging of dislocation motion is one approach to measure dislocation mobility, particularly suited for single crystals. A few dislocations are generated on the surface of a specimen and forced to move in a specific slip direction when the specimen is loaded. Resolving the position of the dislocation either with *in-situ* microscopy (Voisin et al., 2020; T. 2017) or with etch pitting before and after deformation (Alshits et al., 1985; Gorman et al., 1969; Johnston and Gilman, 1959; Vreeland, 1984) can be used to determine the drag coefficient (Jassby and Vreeland, 1973, 1971, 1970; Parameswaran et al., 1972). In high-strain rate deformation experiments such as Kolsky bar tests, the average dislocation velocity (and thus the drag coefficient) can be calculated if the density of mobile dislocations is known *a priori* (Dharan and Hauser, 1973; Kumar et al., 1968; Kumar and Kumble, 1969; Wulf, 1979) or measured *in-situ* (Magagnosc et al., 2021; Nie et al., 2020b). In atomistic simulations, on the other hand, the focus is usually on the motion of a single dislocation on the slip plane (Blaschke, 2019; Blaschke et al., 2021). The ratio of the resolved shear stress to the dislocation velocity is the dislocation drag coefficient, which has been systematically studied over a wide range of stresses and temperatures for pure metals and alloys (Bao et al., 2022; Bitzek and Gumbsch, 2004; Blaschke, 2019; Kuksin et al., 2008; Mordehai et al., 2003; Tian et al., 2023).

These approaches have resolved a number of fundamental concepts pertinent to dislocation drag including different temperature dependencies for different crystal structures in pure metals (Kuksin et al., 2008; Patel and Kalidindi, 2017; Queyreau et al., 2011; Saleh et al., 2019; Wang et al., 2019b) and the role of alloying elements (Blaschke, 2019; Bryukhanov, 2020; Osetsky et al., 2019) on increasing the drag threshold stress and the drag coefficients. Nevertheless, there are inherent limitations associated with them. Direct imaging of dislocations to measure mobility is limited only to materials with low dislocation densities where individual dislocations can be discerned (Al'shitz and Indenbom, 1975). The majority of the atomistic simulations remain focused on idealized microstructural configurations (Kuksin and Yanilkin, 2013). Recently, atomistic-informed multi-scale simulations were shown to be able to capture more complex dislocation configurations (Mayer et al., 2022; Pogorelko and Mayer, 2023). Nevertheless, these approaches are limited to nanometer-sized length scales due to the computational cost. High-strain-rate experiments require a knowledge of mobile dislocation density to quantify dislocation drag (Dharan and Hauser, 1973; Ferguson et al., 1967). Above all is the tacit assumption in all these approaches that the material flow is exclusively governed by dislocation-phonon drag. It may be true that thermal activation is swamped by dislocation drag for extremely high-rate deformations, but it remains nontrivial for the strain rate regime typically probed experimentally for the drag regime, i.e., 10^3 – 10^5 s⁻¹. The question we pose is how to truly isolate the contribution of the dislocation-phonon drag to the plastic flow in metals.

Here we address this question by switching deformation regimes while keeping the deformation length scale and geometry the same. Specifically, we use two impression-based techniques: spherical nanoindentation and laser induced microprojectile impact testing (LIPIT). The former has been routinely used for measurements of material hardness (Jun et al., 2016; Maier et al., 2011; Varam et al., 2014; Zhang et al., 2018). It has been also used to determine constitutive parameters especially when coupled with constitutive modeling schemes (Dean and Clyne, 2017; Jeong et al., 2022; Liu et al., 2020; Lu et al., 2020; Park et al., 2023). The latter is a rather recent development for studies of materials under impact loading (Cai and Thevamaran, 2020; Dowding et al., 2020; Griesbach et al., 2023; Hassani et al., 2023, 2020b; Hassani-Gangaraj et al., 2019, 2018b, 2018c, 2018a; M. 2017; Hyon et al., 2018; Lee et al., 2014, 2012; Thevamaran et al., 2020, 2016; Xue et al., 2017). In LIPIT, a micrometer-sized spherical projectile is launched and impacted onto a target material at high velocities (up to ~1.5 km/s), resulting in characteristic strain rates beyond 10^6 s⁻¹. LIPIT has been used for measuring dynamic hardness of metals (Cai et al., 2023; Hassani et al., 2020a) and constitutive modeling at high rates (Chen et al., 2018; Chen et al., 2023; Larkin et al., 2022; Wang and Hassani, 2020; Xie et al., 2017). The analogy between spherical nanoindentation and LIPIT is clear; the rigid spherical particle as the projectile in LIPIT produces a spherical impression similar to spherical nanoindentation. However, the difference is *mechanistic*. Thermally activated motion of dislocation-phonon drag.

The coupling of nanoindentation and LIPIT, from a modeling point of view, requires the use of constitutive models that can represent multi-strain-rate regimes. Phenomenological models (Baig et al., 2013; Johnson and Cook, 1985; Khan et al., 2004; Khan and Liang, 1999) can provide satisfactory predictions but are not mechanistic. On the other hand, internal state variable models such as dislocation density-based models (Estrin, 1998; Estrin and Mecking, 1984; Mecking and Kocks, 1981; Toth et al., 2002) and the mechanical threshold stress model (Follansbee and Kocks, 1988) are mechanistic, but their applications are limited to strain rates below $10^4 \, \text{s}^{-1}$ (Babu and Lindgren, 2013; Baik et al., 2003; Lemiale et al., 2010; Nemat-Nasser and Li, 1998). Preston-Tonks-Wallace (PTW) model offers accurate predictions of material behavior over decades of strain rates, from 10^{-3} to $10^{12} \, \text{s}^{-1}$, by combining thermal activation at low rates ($<10^4 \, \text{s}^{-1}$) with the power-law behavior at the overdriven shock regime ($>10^8 \, \text{s}^{-1}$) (Preston et al., 2003;

Wallace, 1981). However, the quantification of dislocation-phonon drag using PTW model is not ideal since a physical description of the transitional regime $(10^4-10^8 \text{ s}^{-1})$ is lacking. More recent developments reported dislocation density-based models considering hardening mechanisms stemming from long-range barriers (athermal stress), short-range barriers (thermal activation stress), and dislocation-phonon drag (Austin and McDowell, 2012, 2011; Barton et al., 2011; Gao and Zhang, 2012). While these models provide insight into deformation mechanisms and microstructure evolution, they are expensive to calibrate, typically requiring stress-strain curves at multiple strain rates and temperatures from Kolsky bar tests for strain rates up to 10^4 s^{-1} (Khan et al., 2007; Lee et al., 2006; Lennon and Ramesh, 2004; Morrow et al., 2016; Nemat-Nasser et al., 1999; Nemat-Nasser and Guo, 2000; Nemat-Nasser and Isaacs, 1997), and pressure-shear plate impact tests for strain rates up to 10^6 s^{-1} (Clifton, 1985; Frutschy and Clifton, 1998; Gilat and Clifton, 1985; Klopp et al., 1985; Tong et al., 1992).

In this work, we leverage the mechanistic difference for similar deformation geometry with spherical indentation and LIPIT to quantify dislocation drag. We further analyze the LIPIT data from our previous publication (Hassani et al., 2020a) and produce spherical impressions with comparable volumes using nanoindentation. We precisely measure the plastic work for each impact and indentation impression and show a significant increase for LIPIT impressions compared to spherical nanoindentation impressions. We integrate the classical descriptions of the key deformation mechanisms, athermal hardening, thermal activation and dislocation-phonon drag, along with necessary assumptions to reduce the calibration cost. Our results will demonstrate that, with a limited number of nanoindentation and LIPIT measurements and through a computational cost-effective parameter calibration, this model can accurately predict constitutive parameters for decades of strain rates ranging from quasi-static up to $10^8 \, \text{s}^{-1}$. The integrated experiment and constitutive modeling can precisely quantify the dislocation-phonon drag regime as well as its contribution to plastic flow in metals.

2. Material and method

2.1. Experiment

We chose copper (Cu) as a model FCC metal for this work. A Cu plate purchased from Alfa Aesar (Ward Hill, USA) was cut into 12×12×3.175 mm plates using a precision low-speed diamond saw. The Cu plates were then ground and polished to nominally 0.04 µm surface finish following standard metallography sample preparation procedures. The specimen microstructure was characterized by electron backscatter diffraction (EBSD) using a Zeiss Sigma 500 scanning electron microscope (SEM). A scanning step of 0.13 µm was used to map an area of 39×52 µm for EBSD. Nanoindentation was conducted using a micromechanical testing stage (Alemnis AG, Switzerland) and a 10-µm diameter spherical diamond tip (Fig. 1a). The nanoindentation experiments were conducted under constant strain rates of 1 s^{-1} , 10 s^{-1} and 100 s^{-1} and with a range of indentation depths from 1 to 5 μ m. For the LIPIT experiments, alumina particles purchased from Inframat Advanced Materials LLC (Amherst, USA) were dispersed on top of a launch pad. The launch pad consisted of a 30-um thick polyurea (PU) film, a 60-um gold layer and a 210-um thick glass substrate. A laser pulse (10-ns duration, 532-nm wavelength, pulse energy up to 60 mJ) was focused onto a 50-µm-diameter spot to ablate the sacrificial gold film and consequently expand the PU film, which in turn launched a selected alumina particle. The impact and rebound processes were captured by a high-speed camera (SIMX 16, Specialised Imaging) illuminated by a laser pulse (10-µs duration, 640-nm wavelength). In total, twenty four impact experiments were conducted with particle diameters in the range of 10-19 µm and impact velocities in the range of 175–727 m/s. The impact data produced by LIPIT is taken from our previous publication (Hassani et al., 2020a) and further analyzed here. The spherical impressions were characterized using a Tescan Mira3 high-resolution SEM and a 3D laser-scanning profilometer (Keyence VK-X260). Both LIPIT and nanoindentation were conducted site-specifically to enable us to precisely correlate the characteristics of the impressions (e.g., depth and volume) to the driving parameters (e.g., indentation force, impact velocity, and plastic work).

2.2. Constitutive model

We develop a physically-based constitutive model to account for three main deformation mechanisms following the classic previous

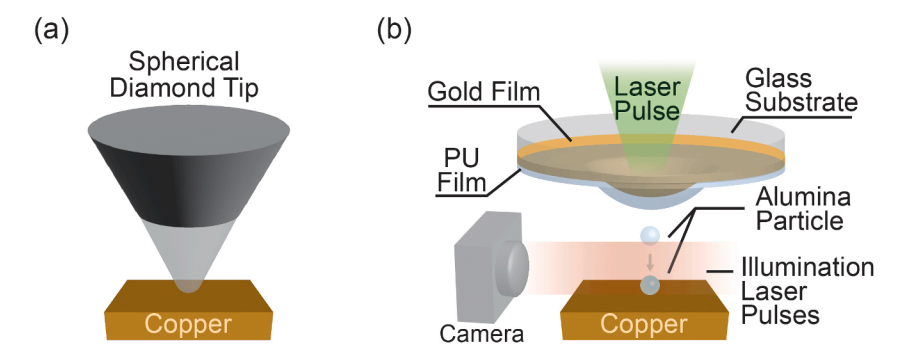


Fig. 1. Schematics of the experimental setups: (a) spherical nanoindentation, and (b) laser-induced microprojectile impact testing (LIPIT).

works (Estrin and Mecking, 1984; Gilman, 1969; Harold and Ashby, 1982; Kocks and Mecking, 2003; Meyers, 1994): athermal hardening, thermally activated dislocation motion, and dislocation drag. We model the flow stress as an additive term considering these three contributions:

$$\sigma = \sigma_a + \sigma_{th} + \sigma_{dt} \tag{1}$$

The additive form of the equation enables us to identify the dominant mechanism and quantify the contribution of each mechanism to the overall material behavior across various strain rates and temperatures.

2.2.1. Thermal activation

When a dislocation bypasses a short-range obstacle (e.g., solute atoms or another dislocation), it moves from one equilibrium position to the next by overcoming an energy barrier associated with the obstacle. A threshold stress, σ_0 , can be defined as the stress required to move a dislocation past the obstacle without thermal energy, i.e., at 0 K. By increasing the amplitude of atomic vibrations at finite temperatures, the thermal activation, ΔG , facilitates the barrier overcoming and thus reduces the required stress (Meyers, 1994):

$$\sigma_{th} = \sigma_0 \left\{ 1 - \left[\frac{\Delta G}{g_0 \mu b^3} \right]^{1/q} \right\}^{1/p} \tag{2}$$

where g_0 is a constant associated with the strength of the obstacles and of the order $0\sim2$ depending on the microstructure (Harold and Ashby, 1982), b is the magnitude of the Burgers vector, μ is the shear modulus, and p and q are constants exponents describing the shape and spacing of energy barriers associated with the obstacles. Cu has an FCC crystal structure in which forest dislocations are the primary short-range obstacles (Meyers, 1994; Nemat-Nasser and Li, 1998). Here p=2/3 and q=2 are used to describe the energy barriers of forest dislocations (Liu et al., 2015a; Nemat-Nasser and Li, 1998). The temperature and rate dependency of the thermal activation can be described as:

$$\Delta G = kT \ln \left(\frac{\dot{\varepsilon}_0}{\dot{\varepsilon}} \right) \tag{3}$$

where \dot{e} and \dot{e}_0 are the imposed and reference strain rates, T is the temperature, and k is the Boltzmann constant. We also treat the shear modulus to be temperature dependent (Varshni, 1970):

$$\mu(T) = \mu_0 - \frac{a}{\exp(T_r/T) - 1} \tag{4}$$

where μ_0 is the shear modulus at 0 K, and a and T_r are constants describing the decay in shear modulus as the temperature increases.

2.2.2. Athermal hardening

In addition to the short-range interactions, the potential field of long-range obstacles such as far-field forest dislocations and grain boundaries provides resistance to dislocation motions (Babu and Lindgren, 2013; Nemat-Nasser and Guo, 2000; Nemat-Nasser and Li, 1998). This resistance depends on the microstructure of the material and is athermal as it cannot be overcome by thermal activation energy:

$$\sigma_a = \alpha \mu b \sqrt{\rho_t} \tag{5}$$

where α is a constant close to unity, and ρ_t is the total dislocation density of the material. Dislocation density evolves through the simultaneous processes of accumulation and annihilation as the material undergoes straining. Moving dislocations can be trapped and accumulate at impenetrable obstacles on their glide planes. The rate at which dislocations accumulate with plastic strain is proportional to the average spacing of dislocations, $\sqrt{\rho_t}$. On the other hand, annihilation takes place by a dynamic recovery process where stored dislocations leave the glide planes by cross-slip or dislocation climb. As a result, the rate of dislocation annihilation is dependent on the total dislocation density with a proportionality that is temperature and strain rate dependent (Agaram et al., 2021). The evolution of the total dislocation density with plastic strain, ε_p , can be modeled as (Estrin, 1996; Estrin and Mecking, 1984):

$$\frac{d\rho_t}{d\varepsilon_p} = k_1 \sqrt{\rho_t} - k_2(\dot{\varepsilon}, T)\rho_t \tag{6}$$

where k_1 is a constant parameter. The second term $k_2(\dot{\epsilon}, T) = k_{20}/r(\dot{\epsilon}, T)$ describes the strain rate and temperature dependency of dynamic recovery with k_{20} being a constant and $r(\dot{\epsilon}, T)$ taking a thermal activation form (Kocks and Mecking, 2003):

$$r = \left\{ 1 - \left[\frac{kT}{g_0 \mu b^3} ln \left(\frac{\dot{\varepsilon}_0}{\dot{\varepsilon}} \right) \right]^{1/q} \right\}^{1/p} \tag{7}$$

2.2.3. Dislocation drag

If the applied stress is large enough, dislocation can bypass obstacles continuously. In this case, dislocations are accelerated to high steady velocities. Fast moving dislocations experience a drag force that is proportional to their velocity. We model the dislocation-

phonon drag by a stress term proportional to the dislocation velocity:

$$\sigma_d = \frac{MvB}{h} \tag{8}$$

where *B* is the phonon drag coefficient. As the amplitude of lattice vibration increases with temperature, we use a temperature-dependent linear form for the drag coefficient (Blaschke et al., 2020; Harold and Ashby, 1982):

$$B = B_0 + B_1 T \tag{9}$$

where B_0 and B_1 are constants. For a given imposed strain rate, $\dot{\varepsilon}$, the average velocity of mobile dislocations is inversely proportional to the mobile dislocation density, ρ_m :

$$v = \frac{M\dot{e}}{\rho_m b} \tag{10}$$

We consider the mobile dislocation density, ρ_m , to be a fraction of the total dislocation density $\rho_m = f\rho_t$. Given that the likelihood of mobile dislocations becoming pinned or trapped increases as the total dislocation density increases, we treat the fraction, f, to be a decreasing function of the total dislocation density with a proportionality coefficient, Φ , (Gilman, 1969, 1965):

$$f_i = f_{i-1} \left[1 - \Phi(\rho_{t,i} - \rho_{t,i-1}) \right] \tag{11}$$

where i and i-1 denote the values of the current and previous time steps respectively. The fraction of mobile dislocation density described by Eq. (11) is implicitly strain-rate dependent due to the strain-rate sensitivity of the evolution of total dislocation density (see Eq. (6)) and decreases as the total dislocation density increases. These behaviors are in accord with previous studies on mobile dislocation density (Gasca-Neri and Nix, 1974; Kumar and Kumble, 1969; Ye et al., 2023).

As the dislocation velocity approaches the shear wave velocity of the material, v_s , it exhibits an asymptotic behavior, ultimately

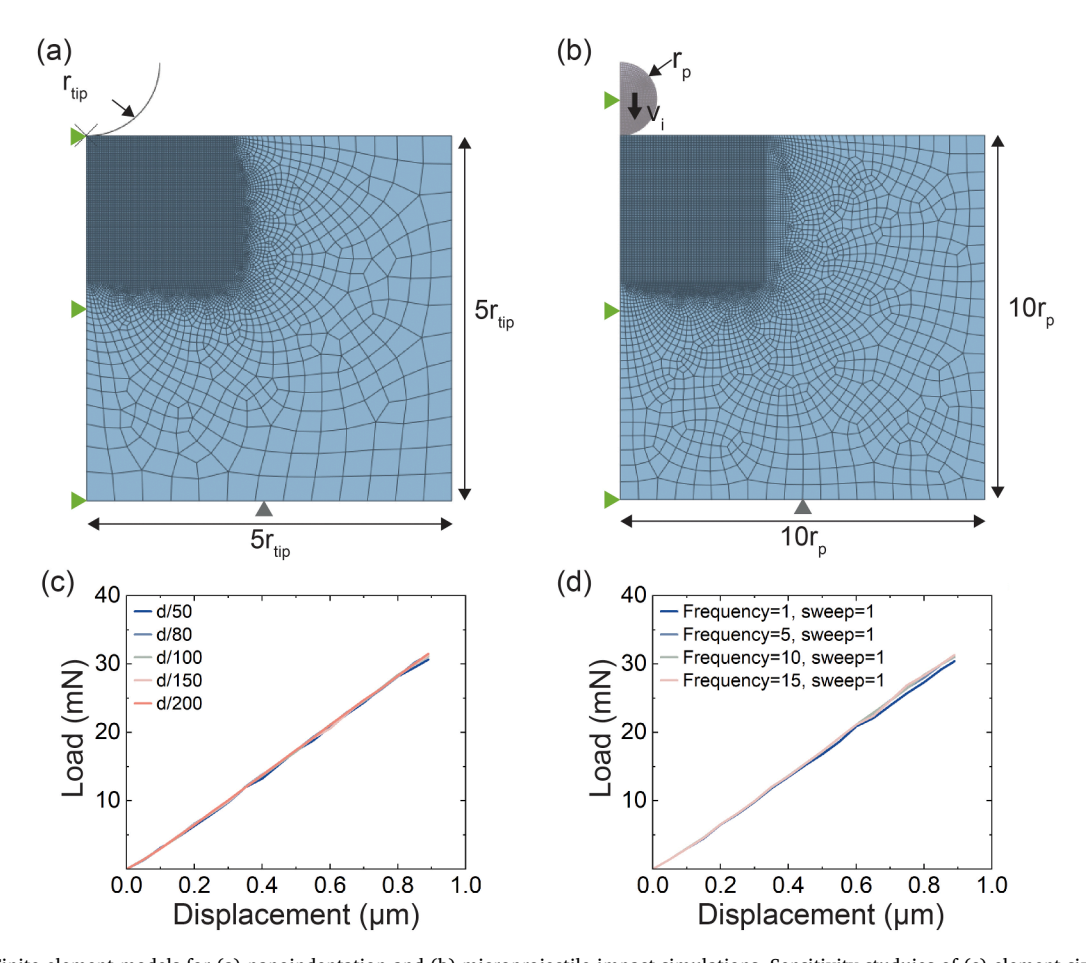


Fig. 2. Finite element models for (a) nanoindentation and (b) microprojectile impact simulations. Sensitivity studuies of (c) element size and (d) adaptive meshing frequency.

converging towards v_s (Meyers, 1994). Here, we simplify this relativistic relation with imposing a discrete upper bound on dislocation velocity:

$$v \le v_s = \sqrt{\frac{\mu}{\rho}} \tag{12}$$

where ρ is the mass density.

Mass inertia can prevent instantaneous acceleration and stopping of a moving dislocation (Regazzoni et al., 1987). Therefore, it can help dislocation overcome short-range obstacles inertially (Granato, 1971). However, this effect is limited to low temperatures (Schwarz and Labusch, 1978). Considering that the dislocation-drag effect will be negligible at such low temperature (T < 50 K for Cu (Schwarz et al., 1977)), the inertia effect is not included in the constitutive model. We have also neglected the effect of twinning with the assumption of a smaller contribution compared to dislocation slip (Liu et al., 2015b; Meyers et al., 2001; Rohatgi et al., 2001). A first order approximation of the effect of twinning on the flow stress (Bouaziz and Guelton, 2001; Moon et al., 2021) based on the reported experimental shock-induced twin volume fraction (Meyers and Murr, 1981) and impact-induced twin thickness (Tiamiyu et al., 2023) in Cu results in only a few percent contribution to hardening for the range of impact velocities studied here. Additionally, we have neglected possible shock hardening effect (Hunter and Preston, 2022; Larkin et al., 2022) in our constitutive model considering the power law decay of the shock intensity with the propagation distance (Zaretsky and Kanel, 2013). While in the conditions of plate impact, the formed plane shock wave is the dominant process, during impact of a finite-size microprojectile, the side (lateral) unloading greatly reduces the shock wave intensity. The main portion of the kinetic energy of the microprojectile is dissipated in the course of localized dynamic severe deformation. A first order approximation of the shock-induced hardening based on the experimental measurements of the dislocation density as a function of shock pressure (Murr, 1988) suggests ~4-8 % contribution to the flow stress for the impact pressure range explored here (see supplementary materials). On these bases, we proceed with the assumption that the majority of strengthening in the present case occurs through athermal, thermal activation, and dislocation drag mechanisms. However, the approach can be in principle extended to capture additional hardening mechanisms and constitutive parameters which we leave to future studies.

2.3. Finite element implementation

We developed a VUHARD subroutine to implement the above constitutive framework in the Abaqus finite element (FE) simulation package (Dassault Systemes, 2019). FE models were developed to simulate nanoindentation and microprojectile impact experiments. The deformation geometry for nanoindentation and LIPIT is similar, as both experiments induce spherical impressions with rigid spherical objects. Therefore, the spherical diamond indenter, the impacting alumina particle, and the resulting impressions can be idealized as axisymmetric and simulated by 2D axisymmetric models. A rigid indenter and a deformable substrate (Fig. 2a) were used for nanoindentation simulations. The displacement of the indenter as a function of time recorded from the experiments was used as a boundary condition for the indenter in the simulations. Microprojectile impact was simulated using a rigid sphere projectile and a deformable substrate (Fig. 2b). Sphere diameters and initial velocities measured from LIPIT experiments were applied for the simulations. The radius and height of the substrate were set as 5 times the indenter radius for nanoindentation simulations and 10 times the sphere radius for impact simulations.

Both indentation and impact simulations were conducted using a thermo-mechanically coupled model. The fraction of plastic work converted into heat is described by the Taylor-Quinney coefficient, which has been reported to be dependent on the material, microstructure, and the deformation process (Lieou et al., 2019; Nieto-Fuentes et al., 2018; Rittel et al., 2017; Salehi and Kingstedt, 2023; Zaera et al., 2013). For Cu, the Taylor-Quinney coefficient varies in the range of 0.4 to 0.95 and increases with strain rate and plastic strain (Rittel et al., 2012; Soares and Hokka, 2021). Considering that the temperature rise is negligible in the nanoindentation, and the strain rate introduced by LIPIT is several orders of magnitude higher than in previous works (up to $10^4 \, s^{-1}$), we assumed a value of 0.9 for Taylor-Quinney coefficient.

Element size sensitivity was investigated using 1- μ m nanoindentation simulations with 1 s^{-1} strain rate (Fig. 2c), with element resolutions ranging from 1/50 to 1/200 of the indenter diameter. The peak load varies within 1 % across all simulations, indicating convergence in predictions. The indenter, the sphere projectile, and the deformation region of the substrate were discretized with an element resolution of d/100, where d is the indenter diameter for nanoindentation simulations and sphere diameter for LIPIT simulations. Adaptive meshing is used to avoid severely distorted elements during simulations. The adaptive meshing frequency sensitivity was assessed by conducting nanoindentation simulations with one remeshing sweep every 1–15 increments (Fig. 2d). Convergence in prediction is observed across all simulations, with the peak load varying within 1.3 %. Therefore, one remeshing sweep per 10 increments was used in nanoindentation and LIPIT simulations.

Previous work shows that the nanoindentation load-displacement prediction is insensitive to friction coefficient until reaching large indentation depths, approximately $50 \, \mu m$ (Jeong et al., 2020). The friction coefficient has been also shown to have a minor effect on plastic strain and temperature in microprojectile impact simulations (Li et al., 2009). The frictional dissipated energy is a very small fraction of the total internal energy when the friction coefficient is set to be 0.4 (Li et al., 2009). Therefore, contact was assumed to be frictionless for both indentation and impact. The substrate bottom was constrained against all degrees of freedom, and the initial temperature was set to 298 K.

3. Results and discussions

3.1. Microstructure characterizations

Fig. 3a shows an inverse pole figure map of the Cu target microstructure. A threshold angle of 2° was used in determining the boundaries. We have measured the average grain size to be $5.91\pm2.21~\mu m$. The distribution of misorientation angle is shown in Fig. 3c, in which we observe two peaks around 4° and 58° . This feature was reported for deformed materials (Elizalde et al., 2020; Zolotorevsky et al., 2019) and can be attributed to the processing of the Cu plate.

3.2. Spherical nanoindentation and microprojectile impact

Fig. 4a shows load-displacement data obtained for different indentation depths at the strain rate of $1 \, \mathrm{s}^{-1}$. We measured the plastic work for each indentation by measuring the area enclosed by the loading and unloading curves. The impression volumes were measured using a 3D laser-scanning profilometer. The base surface is set such that the conservation between pile-up volume and indentation volume is satisfied (Cai et al., 2023; Hassani et al., 2020a). Fig. 4b shows the plastic work per unit volume of indentation as a function of the indentation depth for the indentations conducted at the strain rate of $1 \, \mathrm{s}^{-1}$. We have also measured plastic work per unit volume for 1- μ m indentations at different strain rates (see Fig. 4c). We observe an increasing trend for the plastic work per unit volume as a function of both indentation depth and strain rate, which we attribute to strain hardening and strain rate hardening respectively. Our results can be fitted with power laws with weak exponents, i.e., 0.05 for indentation depth and 0.015 for strain rate. Specifically, the latter correlates well with the experimental measurements of strain rates sensitivities for Cu in the thermal activation regime (Follansbee and Kocks, 1988).

Fig. 5a shows exemplar snapshots for a 13.5- μ m alumina particle impacting a Cu substrate at 727 m/s. Microprojectile impact and rebound velocities were measured in real time and used to calculate the ratio between the two, known as the coefficient of restitution (CoR). Fig. 5b shows the CoR as a function of impact velocity for twenty four such impacts in a wide range of impact velocities. We observe a decreasing trend for CoR approaching a plateau as impact velocity increases. Using the real time measurements of the impact and rebound velocities, we can precisely determine the plastic work done during each impact induced deformation by Eq. (13), where E_{impact} and $E_{rebound}$ are the kinetic energies of the alumina particle during impact and rebound, and v_i and v_r are impact and rebound velocities respectively (Hassani et al., 2020a). Because we do not observe any flattening nor fracture in the alumina particles, we attribute the change in the kinetic energy exclusively to plastic work. Fig. 5b also shows the plastic work normalized by the impression volume. Despite the data scatter due to the microprojectile size variation (ranging from 10.3 μ m to 19 μ m), there is a gradual increase in the normalized plastic work as the impact velocity increases. We attribute this trend to the fact that impacts at higher velocities

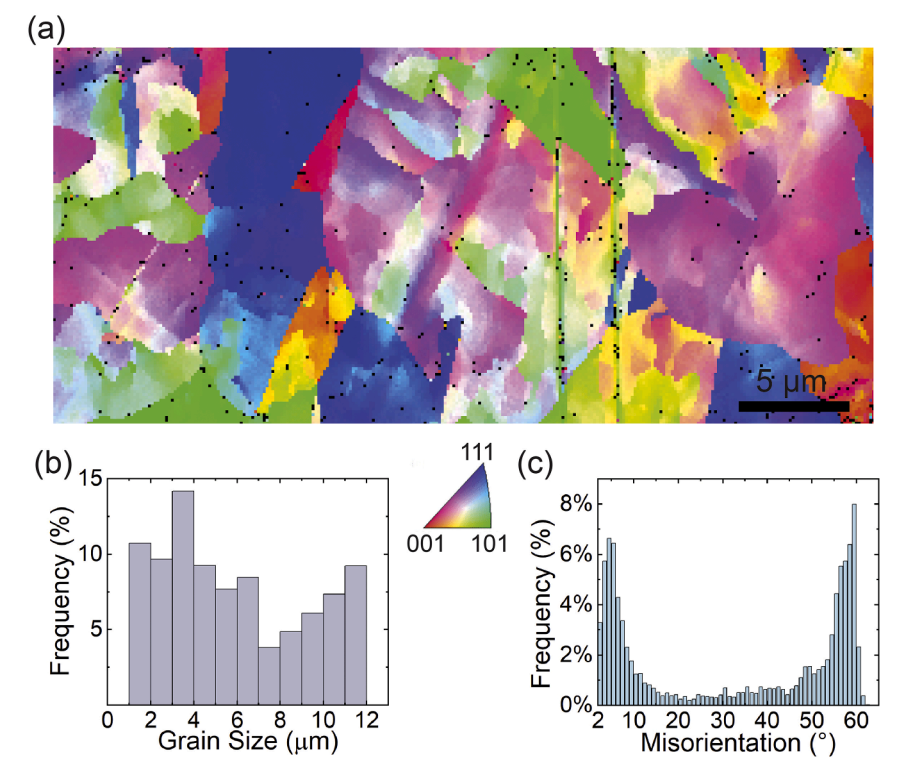


Fig. 3. (a) Microstructure of the Cu target, (b) distribution of grain size, (c) distribution of misorientation angle.

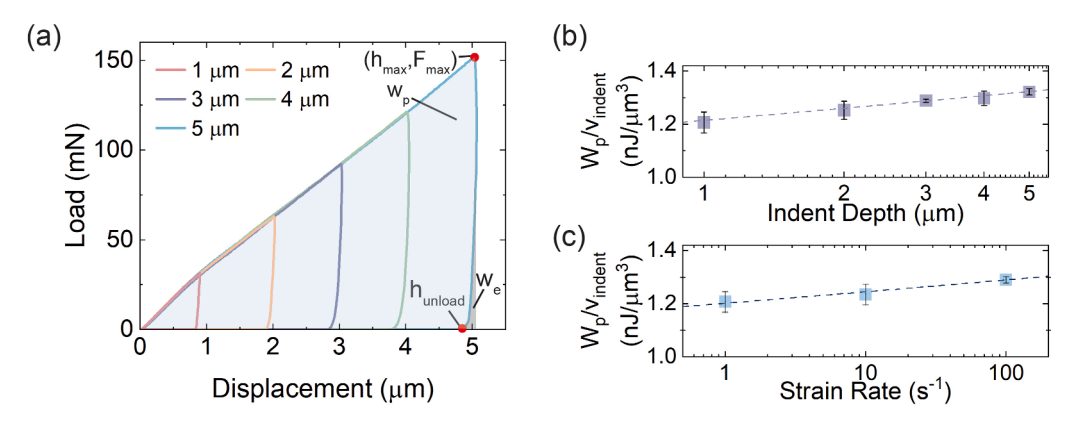


Fig. 4. (a) Load-displacement curves from nanoindentations with various indentation depths and a constant strain rate of $1s^{-1}$ (W_e and W_p are the elastic and plastic works respectively). Plastic work per indentation volume as a function of (b) indentation depth for $1 s^{-1}$ strain rate and (c) as a function of strain rate for 1-μm indentation depth.

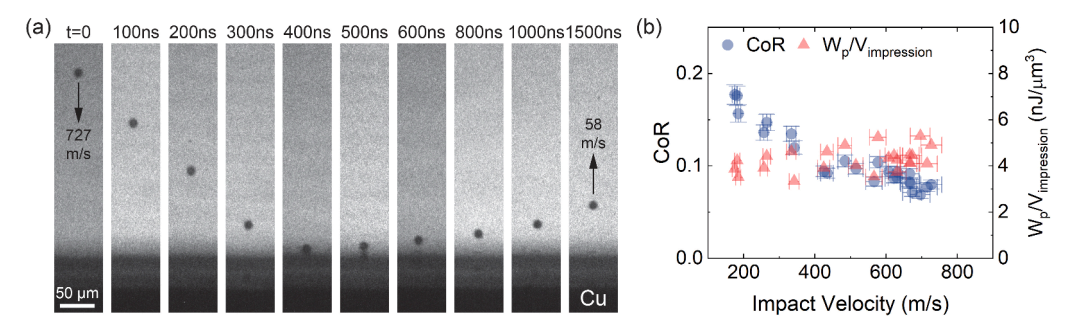


Fig. 5. (a) Multi-frame sequences with 5-ns exposure times showing a 13.5-µm alumina microprojectile impacting a Cu substrate at 727 m/s. (b) Coefficient of restitution (CoR) and the plastic work normalized by the impression volume as a function of impact velocity.

deform the Cu substrate to higher strains and at higher strain rates, during which a higher resistance to plastic deformation is expected. Additionally, the plastic work per unit deformation volume of LIPIT is $3\sim4$ times higher than that of nanoindentation, primarily because the material deforms at much higher strain rates.

$$W_p = E_{impact} - E_{rebound} = \frac{1}{2} m_p \left(v_i^2 - v_r^2 \right) \tag{13}$$

3.3. Plastic work in different mechanistic regimes

The plastic work is a critical parameter that enables direct comparison of spherical nanoindentation with spherical microprojectile impact. Fig. 6a and 6b show the morphology of the two impressions produced by nanoindentation and impact. Fig. 6c and 6d show the reconstruction of the same impressions with laser confocal microscopy. The two impressions have the same depth (3 μ m), closely-matched impression profiles (see Fig. 6e), and comparable volumes, i.e., 98 μ m³ for nanoindentation and 104 μ m³ for impact. The only notable difference is the strain rate at which plastic deformation occurred to generate these two impressions. The impression in Fig. 6a was created by nanoindentation at a constant strain rate of 1 s⁻¹. The nominal average strain rate in microprojectile impact is estimated as $\dot{\epsilon} = v_i/d$, where v_i is the impact velocity, d is the particle diameter. The impression in Fig. 6b was produced by a 10- μ m alumina particle impacting Cu at 696 m/s, resulting in a nominal average strain rate on the order of ~10⁸ s⁻¹. The significantly different strain rate regimes result in significantly different plastic works to create a similar impression; we measured 140 nJ and 553 nJ plastic work for the indentation and impact impression respectively. This is a significant increase in plastic work for the same volume which we attribute to the dislocation-phonon drag mechanism that is absent in nanoindentation but operative during impact.

Measuring plastic work for all the nanoindentation and impact experiments and plotting it as a function of impression volume in Fig. 7 clearly separates the two strain-rate regimes. The plastic work increases with the impression volume for both indentation and impact. However, it is consistently higher for impact over the impression volume range studied here (40 to $550 \mu m^3$). Dislocation-phonon drag is the primary mechanism responsible for the significant difference observed between the two sets of plastic work. Our approach therefore provides an experimentally measurable index that can isolate the dislocation drag effect and will be the basis for the constitutive modeling (next section) to quantify it.

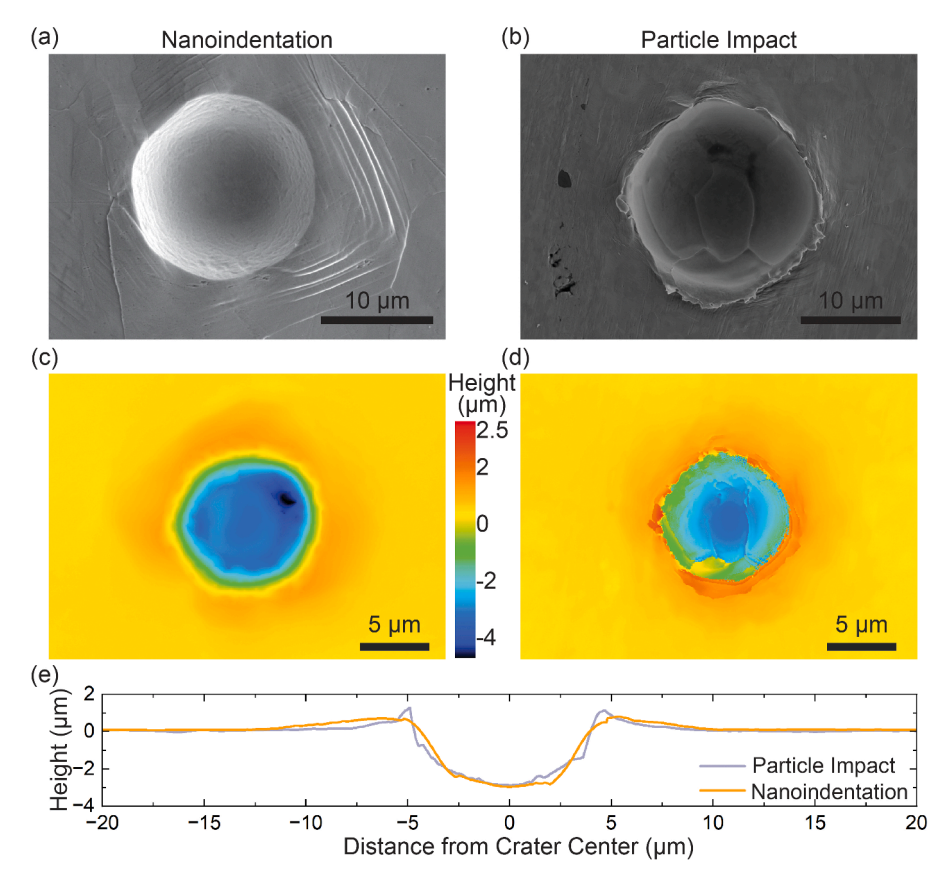


Fig. 6. (a,b) Scanning electron micrographs and (c,d) laser confocal microscopy reconstructions of two impressions produced by (a,c) spherical nanoindentation at 1 s $^{-1}$ strain rate and (b,d) laser-induced microprojectile impact at 696 m/s. (e) Comparison of the geometry of the two impressions. The two impressions are spherical and have similar depths but consumed significantly different plastic works: 140 nJ for nanoindentation and 553 nJ for impact.

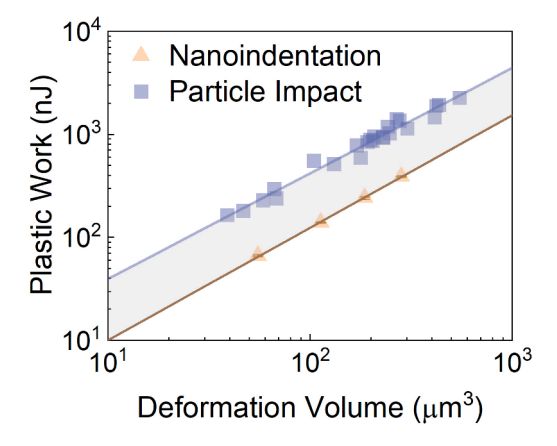


Fig. 7. Plastic work as a function of impression volume clearly separates the two mechanistic regimes for microprojectile impact ($\dot{\epsilon} > 10^6 \text{s}^{-1}$) and in nanoindentation ($\dot{\epsilon} = 1\text{s}^{-1}$).

3.4. Constitutive model calibration

We conduct the constitutive model calibration in two steps. First, the athermal and thermal constitutive parameters are calibrated using 1- μ m nanoindentation experiments at 1 s⁻¹ and 100 s⁻¹ strain rates and validated with nanoindentation at the 10 s⁻¹ strain rate. Next, the dislocation drag constitutive parameters are calibrated using LIPIT measurements. Based on the indent depth and assuming a perfect spherical shape for the indenter, we estimate the width of the 1- μ m nanoindentation impression to be 6 μ m, which is

comparable to the average grain size. Since the size of the indentation-induced plastic zone is approximately 2.4 times the radius of the contact area (Mohan et al., 2021) we can conclude the even the shallowest indentation and impact impressions in the present work have involved several Cu grains in the plastic zone. In fact, our simulations show that, for example, the volume of the plastic zone for impact velocities of 175 and 666 m/s with a 17-µm projectile is 4380 and 29,177 µm³, respectively. Considering the average grain size in the Cu target, these plastic volumes engage 40 and 270 grains for the low and high velocity impacts. This makes the choice of a continuum framework for constitutive modeling reasonable. Our choice is also motivated by the negligible orientation effect reported for the coefficients of restitution measured for microprojectile impacts on FCC single crystals (Cai et al., 2023), as well as by several continuum simulations for constitutive modeling based on microprojectile impacts on metals(Chen et al., 2023; Larkin et al., 2022; Rahmati et al., 2021; Rahmati and Jodoin, 2020; Wang and Hassani, 2020; Xie et al., 2017). Furthermore, Nguyen et al. (2017) proposed that all possible slip systems can be activated during the spherical cavity growth and applied a modified J2 theory to predict this process, which was shown to agree well with direct numerical simulations. Creating spherical impressions in a Cu substrate through nanoindentation and LIPIT is analogous to spherical cavity growth, further supporting the use of a continuum approach.

In both calibration steps (indentation and LIPIT), we use iterative FE simulations coupled with genetic algorithms (GA) to minimize an error function. GA generates an initial population of trial parameter sets that map the space defined by the lower and upper bounds for each constitutive parameter. The trial parameter sets are then used in FE simulations to predict the deformation behavior. The parameter sets that minimize the error between experiments and predictions are then used to create the next generation of parameter sets through crossover and mutation (Melanie, 1996). Each generation includes 50 trial parameter sets. The optimization is done iteratively until the same minimum error is resulted after five consecutive generations.

Starting with the nanoindentation experiments, the FE-predicted, and experimental load-displacement data was discretized into 50 data points along the loading curve, and a mean absolute percentage error (MAPE) is defined as the error function:

$$MAPE = \frac{\sum_{i}^{n} \frac{\left|F_{FE,i} - F_{exp,i}\right|}{F_{exp,i}}}{n} \tag{14}$$

Where n=50 is the number of discretized data points, and $F_{FE,i}$ and $F_{exp,i}$ are the predicted and experimental loads at each point. The athermal constitutive parameters, k_I and k_{20} , and the thermal activation constitutive parameters g_0 and σ_0 , were optimized by GA to minimize the error function. After the calibration, FE prediction for the 10 s^{-1} nanoindentation was conducted to validate the constitutive parameters set. A comparison of the predicted and measured load-displacement curves for 1 s^{-1} , 10 s^{-1} , and 100 s^{-1} nanoindentations are shown in Fig. 8. While it is expected to observe good match for the 1 s^{-1} and 100 s^{-1} cases because they have been used in the calibration procedure, the reasonable agreement between the experimental and predicted load-displacement data for the indentation with 10 s^{-1} strain rate serves as validation for the athermal and thermal constitutive parameters calibration.

Moving to microprojectile impact, we used both experimentally measured CoR and impression depth in a weighted form to define the error function. CoR reflects the portion of the kinetic energy consumed during deformation, which is influenced by both material strength (hardening) and the deformation volume. Therefore, we include impression depth as part of the error function to account for the impression size effect on the material hardening.

$$MAPE = \frac{\sum_{i}^{n} \left(w \times \frac{\left| CoR_{FE,i} - CoR_{cop,i} \right|}{CoR_{cop,i}} + (1 - w) \times \frac{\left| h_{FE,i} - h_{cop,i} \right|}{h_{cop,i}} \right)}{n}$$

$$(15)$$

In Eq. (15), n is the number of impact experiments used in the calibration, w and (1-w) is the weights assigned for the CoR and the impression depth respectively. Considering that the CoR is the in-situ measurement of material dynamic behavior, which is the focus of the calibration, we assign a higher weight of 0.8 to the CoR in the calibration. We set the weight of impression depth to be 0.2 as it is

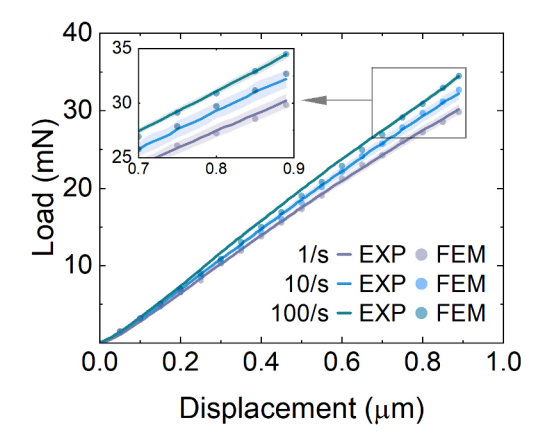


Fig. 8. Comparison of the experimental measurements and finite element predictions of the load-displacement curves for 1- μ m indentations at constant strain rates of 1 s⁻¹, 10 s⁻¹ and 100 s⁻¹.

introduced as an additional constraint to the calibration results. Eight impact experiments were selected for model calibration, which span the explored particle size range (13–19 μ m) and the impact velocity range (175–716 m/s). The results for the remaining impact experiments were used for validation. Fig. 9a shows a comparison between the experimental and the predicted plastic work per unit particle volume as a function of impact velocity. Fig. 9b compares the experimental and the predicted impression depths normalized with the diameter of the impacting particles as a function of impact velocity. Both the eight impacts used for calibration and the remaining sixteen impacts used for validation show good agreement between the measured and simulated responses, which validate the calibrated dislocation drag constitutive parameters, B_0 , B_1 and Φ .

Table 1 summarizes the material parameters used in the model together with the calibrated parameters. For microstructures having forest dislocations as the primary source of short-range barriers, the range of g_0 is typically 0.2–1 (Harold and Ashby, 1982). Our g_0 calibration falls into this range and is closer to the upper bound which aligns with the EBSD analysis of a complex dislocation structure with relatively high dislocation density. k_I has been reported as 680 um⁻¹ for Cu (Liu et al., 2015a) and 568 um⁻¹ for SS304 alloy (Liu et al., 2014). The value resulting from our calibration deviates from previous works since k_I is microstructure dependent. However, it exhibits comparable orders of magnitude. Direct comparison of k_{20} is not applicable as the prior works (Liu et al., 2015a, 2014) used different models for dislocation annihilation. The calibration results for the phonon-drag coefficient and the threshold stress are discussed in Section 3.5. The initial dislocation density (ρ_{t0}) was estimated by an empirical relationship, $d_0 = k_0/\sqrt{\rho_{t0}}$ (Lemiale et al., 2010), where k_0 is a constant and was determined to be 19.1 for Cu using grain size and dislocation density measurements by Hu et al. (2017). Based on the average grain size characterized in Section 3.1, an initial dislocation density of 10^{13} m^{-2} was used in our simulations. The initial fraction of the mobile dislocations is challenging to measure experimentally and has been assumed to be 0.5 to fit the LIPIT observations shown in Fig. 9.

3.5. Quantifying dislocation drag

The constitutive modeling approach described above together with the nanoindentation and microprojectile impact experiments enable us to isolate and quantify the dislocation drag behavior. Fig. 10 shows the phonon drag coefficient quantified with our approach compared to those from literature using experiments or molecular dynamics (MD) simulations. While the impact experiments were conducted at room temperature, the impact-induced adiabatic temperature rise captured in our thermo-mechanically coupled FE simulation enables us to determine the temperature dependency of the dislocation drag within the temperature range recorded in our impact simulations (the solid black line). Our results correspond well with both experimental measurements and MD predictions, not only within the explored temperature range, but also when extrapolated to higher or lower temperatures. Specifically for low temperatures, while we have not imposed a zero intercept in the model (see Eq. (9)), our model predicts insignificant drag coefficients. This matches the expected behavior for FCC metals that the drag coefficient vanishes as the temperature approaches 0 K. For example, drag coefficients on the order of 10^{-6} Pa.s have been measured for Cu and aluminum (Al) at 4.2 K (Hikata et al., 1970; Jassby and Vreeland, 1973). Similarly, MD simulations predict drag coefficients in Cu and Al approaching zero with the decrease in temperature (Bitzek and Gumbsch, 2004; Kuksin and Yanilkin, 2013; Oren et al., 2017). This behavior is attributed to suppressed thermally activated atomic vibrations at extremely low temperatures (Kuksin and Yanilkin, 2013), and is captured with our approach.

We also quantified the thermal activation threshold stress (σ_0) to be 551 MPa. The threshold stress depends on the initial configuration of forest dislocations in FCC metals. Different dislocation structures resulting from different processing conditions (Landau et al., 2009; Yang et al., 2021) makes a direct comparison of this parameter from one study to another challenging. Nevertheless, we observe a logical pattern when comparing our thermal activation threshold stress with literature data. For perfectly annealed Cu, the threshold stress ranges from 40 to150 MPa (Hu et al., 2017; Nemat-Nasser and Li, 1998), while for as-processed (deformed) Cu plate with a grain size of 30–40 μ m, the threshold stress falls within the range of 114–400 MPa (Follansbee and Kocks, 1988; Gourdin and Lassila, 1992; Nemat-Nasser and Li, 1998). The threshold stress predicted in this work is higher than these measurements which we attribute to the smaller grain size (5.91 μ m) in our Cu plate compared to other works.

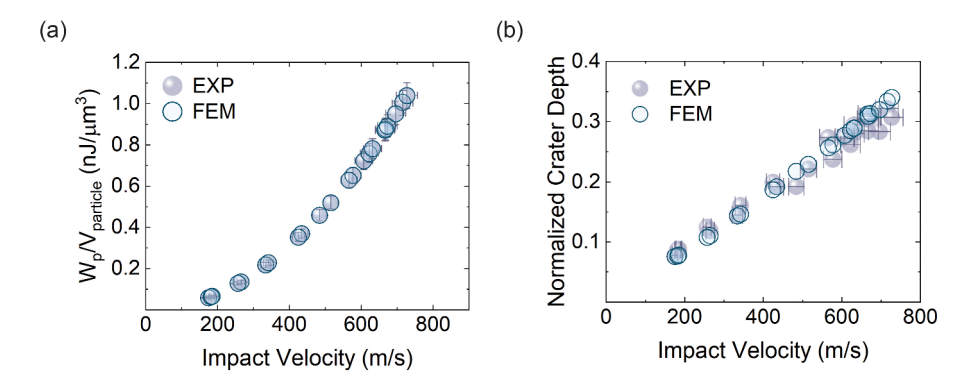


Fig. 9. Comparison of the experimental measurements and finite element predictions of (a) impact-induced plastic work and (b) impact-induced impression depth as functions of impact velocity.

Table 1 Material parameters for Cu.

Known		Calibrated	
μ_0 , GPa	45.73	k_I , $\mu \mathrm{m}^{-1}$	141.55
a, GPa	3.62	k_{20}	2.08
T_r , K	207.9	g_O	0.93
b, μm	0.000256	σ_0 , MPa	551.5
$\dot{\varepsilon}_0$, s^{-1}	2×10^{10}	B₀, Pa·s	8.18×10^{-8}
k, nJ/K	1.38×10^{-14}	B₁, Pa·s/K	6.67×10^{-8}
p	0.67	Φ , μ m ²	0.0035
\overline{q}	2		
α	0.765		
M	3.06		
ρ_{mass} , g/cm ³	8.96		
ρ_{t0} , $m = 2$	10^{13}		
fo	0.5		

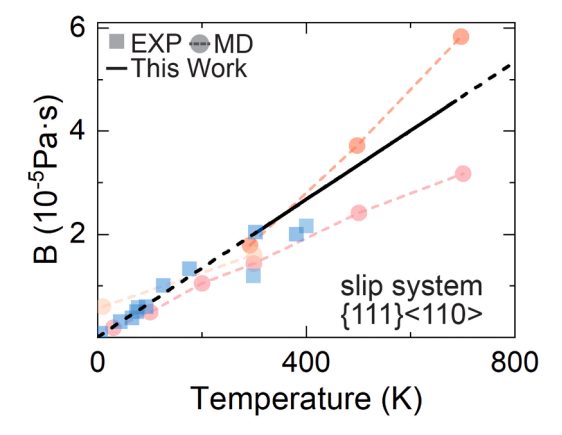


Fig. 10. Comparison of the quantified phonon drag coefficient with previous experimental measurements and atomistic simulations (Bitzek and Gumbsch, 2004; Jassby and Vreeland, 1973; Kuksin and Yanilkin, 2013; Mayer et al., 2022; Oren et al., 2017; Suzuki et al., 1964).

3.6. Dislocation velocity

The average dislocation velocity as a function of the flow stress are shown in Fig 11 for two conditions of flow stress with and without the dislocation-phonon drag contribution. The temperature and dislocation density are set as 300 K and $10^{13} \, m^{-2}$ respectively. For both cases, the dislocation velocity is negligible under low stresses and starts to accelerate with increasing stress. The difference arises when the stress approaches the threshold stress (Regazzoni et al., 1987). The velocity shows an abrupt acceleration toward infinity when dislocation-phonon drag is absent. However, in the presence of dislocation-phonon drag, the dislocation velocity

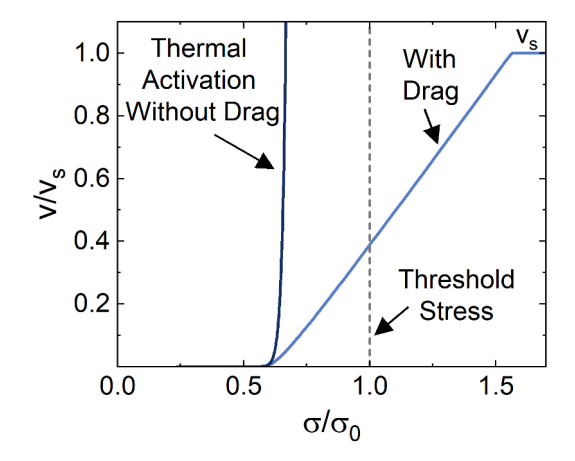


Fig. 11. Stress dependence of the average dislocation velocity.

increases more gradually and shows a linear relationship to the flow stress at high flow stress region ($\sigma/\sigma_0 \ge 1$). Because of the assumption in Eq. (12), the relativistic effect is not captured by the model, and thus the dislocation velocity reaches to an upper limit when $\sigma/\sigma_0 \approx 1.56$.

3.7. Thermal activation vs. dislocation drag: mechanistic contributions

We chose impressions created by microprojectiles of similar sizes but different velocities for a detailed analysis of the mechanistic contributions to impact-induced deformation. Fig. 12a shows the laser confocal microscopy reconstruction of the three impressions. As impact velocity increases, the impression depth, width, and volume increase. Our finite element simulations also show the same trend. The plastic flow in all these cases is accommodated by \sim 2 orders of magnitude increase in the total dislocation density. For the low impact velocity (175 m/s), dislocation density increases from 10^{13} m $^{-2}$ to 10^{15} m $^{-2}$, while for medium impact velocity (434 m/s), the increase is much higher resulting in a maximum dislocation density of 2×10^{15} m $^{-2}$. We do not observe a significant increase in the total dislocation density from the 434 m/s impression to the 666 m/s. In fact, there is a subtle decrease in the maximum total dislocation density at the pile-up region, which we attribute to the adiabatic temperature rise in that localized deformed region. In the central regions where the adiabatic temperature rise is not as severe, the dislocation density continues to increase from 434 to 666 m/s. Overall, the results are in qualitative agreement with the measurements of geometrically necessary dislocations for impact-induced impressions on single crystal Al (Cai et al., 2023) where dislocation densities of 10^{14} , 2×10^{14} and 1.8×10^{14} m $^{-2}$ were reported for impact velocities of 125, 353, and 550 m/s. These densities are an order of magnitude lower compared to our predictions, which we attribute to much lower initial dislocation density in a single crystal Al compared to our polycrystalline Cu with 5.91 µm average grain size. Nevertheless, the overall trend and subtle decrease in the maximum dislocation density from medium impact velocity to the highest is what we also observe in our simulations.

To find the contribution of different mechanisms to the plastic flow, we compute the increment of plastic work for every element at every time increment in our FEM model:

$$\Delta W = \sigma \times \Delta \varepsilon \times V \tag{16}$$

where $\Delta \varepsilon$ is the incremental plastic strain, V is the element volume, and σ is the flow stress for every element at each time increment. We also compute the strain rate and associate it to the plastic work at every increment. This approach enables us to fractionalize the plastic work done by each mechanism at different strain rates. Fig. 12c shows the contributions from athermal hardening, thermal

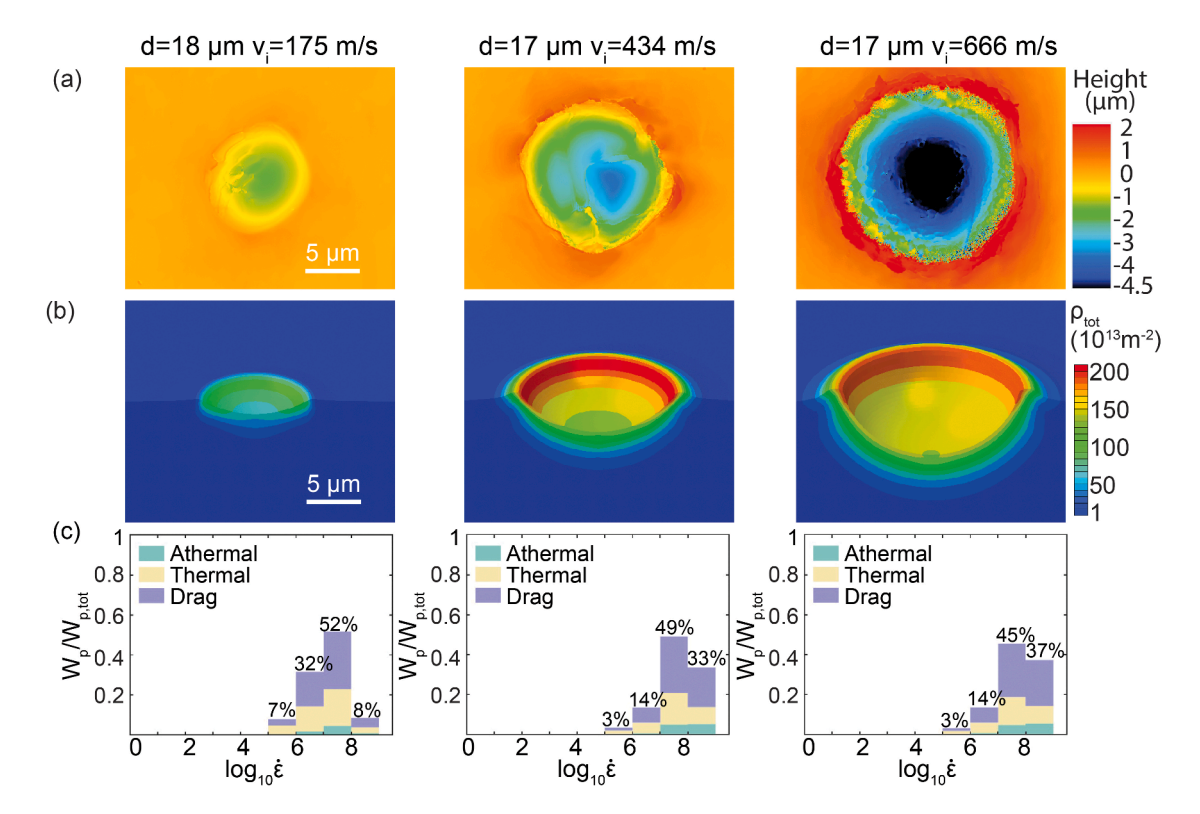


Fig. 12. (a) Laser confocal reconstruction of the impact-induced impressions, (b) finite element predictions of the impact-induced deformation and the distributions of total dislocation density, and (c) mechanistic contributions by athermal, thermal activation and dislocation drag mechanisms to the overall plastic work for three impact velocities: 175, 434, and 666 m/s.

activation, and dislocation drag for the three impact velocities. The fraction of the plastic flow at strain rates smaller than $10^5 \, \mathrm{s}^{-1}$ is less than 1% in all these cases. The majority of plastic deformation takes place at strain rates on the order $10^7 \, \mathrm{s}^{-1}$. We also observe a significant increase in the plastic deformation at strain rates on the order of $10^8 \, \mathrm{s}^{-1}$, from 175 to 434 m/s, followed by a more gradual increase from 434 to 666 m/s. From a deformation mechanism perspective, we observe that while high-strain-rate deformation is primarily dominated by dislocation drag, notable contributions from other mechanisms are also present. The overall contribution of dislocation drag increases from 54 % to 57 % to 59 % as impact velocity increases from 175 to 434 to 666 m/s. We still observe a significant contribution from thermal activation, i.e., 39 %, 32 %, and 30 % respectively. This is driven by the strain rate dependency of this mechanism. The overall contribution of athermal hardening aligns with the evolution of dislocation densities, increasing from 7.5 % to 11 % as the impact velocity increases from 175 m/s to 666 m/s.

3.8. Deformation mechanism maps

Using the results of our integrated experimental and computational framework, we can now develop precise deformation mechanism maps for Cu. One example for a constant microstructure and strain is shown in Fig 13a. While our focus in this work is the transition from the thermal activation to the dislocation drag regime, we have also calculated and included the creep regime in Fig. 13a for the sake of completeness following Ashby's approach (Harold and Ashby, 1982). Diffusion is not included in this map as it is operating in extremely low strain rates (Harold and Ashby, 1982). In finding the rate limiting mechanism between dislocation-glide plasticity and creep, we determined the operative mechanism as the one requiring less stress under the same temperature and strain rate conditions. We used our constitutive model for the transition from thermal activation to dislocation drag. The mechanism that offers the highest contribution to the flow stress is considered as the dominant mechanism. We overlay the map with contours of normalized shear stress, $\tau_n = \tau/\mu$, to delineate the isostress loci within each deformation regime.

In addition to providing a quantitative map for plastic deformation, we find the following behaviors worthy of discussion. First, increasing temperature has opposite effects in the thermal activation and the dislocation drag regimes. In the former, it results in a decrease in the flow stress by providing a higher thermal activation energy. In the latter, however, it results in a higher drag coefficient (see Eq. (9)) and thus increases the flow stress. This competing effect can justify the slight increase in the dislocation drag contribution (5 %) from 175 m/s to 666 m/s (see Fig. 12c). Impacts at higher velocities induce higher rates but also results in higher temperatures. Second, a closer look at the boundary between the thermal activation and the dislocation-phonon drag regime in Fig. 13b shows a very gradual rather than a sharp transition. The contours in Fig. 13b represent the ratio of the dislocation drag stress to the overall flow stress. For example, at room temperature ($T_{homologous} = 0.22$), for strain rates less than $10^5 \, s^{-1}$, thermal activation stress contributes more than 90 % of the flow stress. It takes ~ 2 orders of magnitude increase in strain rate for the dislocation drag stress contribution to increase from 10 % to 90 %. This diffuse transition is in contrast to the commonly held view that this mechanistic transition occurs within one order of magnitude strain rate ($\sim 10^3 \, s^{-1}$). And lastly, due to the reversed temperature effect in thermal activation and dislocation drag, we observe that the ~ 2 orders of magnitude strain rate transitional region gradually shift from $> 10^7 \, s^{-1}$ at cryogenic temperatures to $10^4 - 10^6 \, s^{-1}$ at high homologous temperatures. It is our hope that the proposed approach to study the dislocation-phonon drag regime helps provide a better understanding of this important yet relatively underexplored regime of plastic deformation.

4. Conclusion

We developed an impression-based approach combining laser-induced microprojectile impact and spherical nanoindentation to study the dislocation-phonon drag regime at high strain rates. Additionally, we developed a constitutive framework that, when integrated with the indentation and impact experiments, can quantify the dislocation-phonon drag regime. Based on the results presented in this work the following conclusions can be made:

- Similar deformation geometries and length scales but different operative mechanisms during spherical nanoindentation and microprojectile impact can be leveraged to isolate and study the dislocation-phonon drag regime.
- For similar impression volumes the plastic work during impact is significantly larger than the plastic work during indentation. Specifically for Cu, we measured a fourfold increase in plastic work per unit impression volume during impact compared to spherical nanoindentation.
- While microprojectile impact was conducted at room temperature, the associated adiabatic temperature rise can be leveraged to quantify the temperature dependency of the dislocation-phonon drag coefficient. Specifically for Cu, we quantified the dislocation phonon drag coefficient ranging from 2×10^{-5} Pa.s at room temperature to 4.6×10^{-5} Pa.s at 686 K.
- Plastic deformation during microprojectile impact primarily takes place at strain rates beyond 10⁶ s⁻¹. Approximately 50% of the plastic work takes place at strain rates on the order of 10⁷ and 10⁸ s⁻¹.
- Using finite element simulation and the calibrated constitutive model, we quantified the contribution of the individual deformation
 mechanism to the overall plastic work during laser-induced microprojectile impact. Although dislocation-phonon drag emerged as
 the predominant deformation mechanism, contributing more than 50 %, a substantial contribution from thermal activation
 (approximately 30 %) was also identified, owing to the combined strain rate and temperature dependencies associated with this
 mechanism.
- Based on our constitutive modeling we developed a deformation map for Cu focusing on the transition from thermal activation to
 dislocation-phonon drag. We found a gradual rather than a sharp transition. It takes roughly two orders of magnitude increase in
 strain rate for the contribution of the dislocation-phonon drag to increase from 10 % to 90 %. An increase in temperature results in

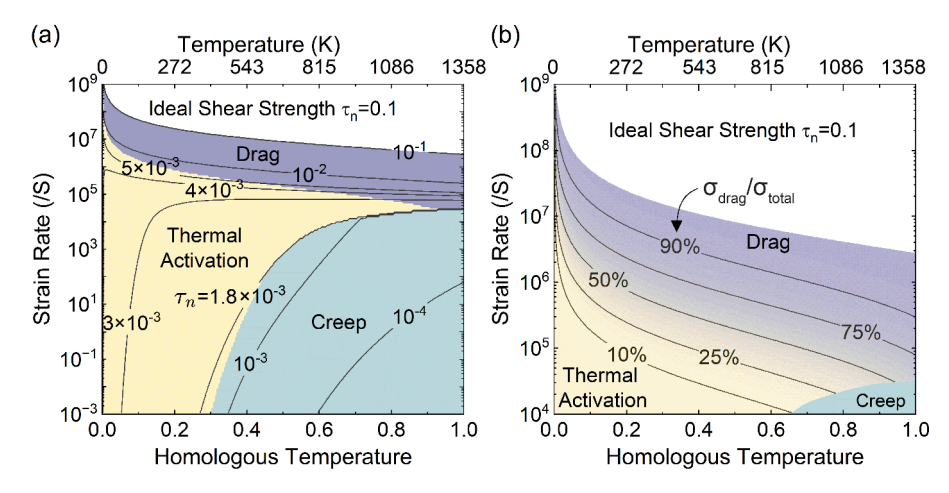


Fig. 13. Deformation mechanism map for copper (a) showing thermal activation-controlled plasticity, drag-controlled plasticity, and creep regimes and (b) focusing on the transition from the thermal activation to the dislocation-phonon drag regime.

softening in the thermal activation regime but hardening in the dislocation-phonon drag regime. With increasing temperatures, the threshold strain rates for the transition from thermal activation to dislocation drag decrease.

Overall, we proposed and demonstrated an impression-based approach combining laser-induced microprojectile impact and spherical nanoindentation to isolate dislocation drag at high strain rates experimentally. We have also proposed and applied a continuum constitutive modeling approach to quantify the dislocation-phonon drag regime. Extending the framework to include additional hardening mechanisms or coupling it with crystal plasticity could provide more insights into the high strain rate deformation of metals which we propose as directions for future studies.

CRediT authorship contribution statement

Qi Tang: Writing – original draft, Validation, Investigation, Formal analysis, Data curation. **Mostafa Hassani:** Writing – review & editing, Supervision, Methodology, Funding acquisition, Conceptualization.

Declaration of competing interest

The authors declare that they have no known competing financial interests or personal relationships that could have appeared to influence the work reported in this paper.

Data availability

Data will be made available on request.

Acknowledgment

The authors gratefully acknowledge the funding received by the National Science Foundation CAREER Award (CMMI- 2145326).

Supplementary materials

Supplementary material associated with this article can be found, in the online version, at doi:10.1016/j.ijplas.2024.103924.

References

Agaram, S., Kanjarla, A.K., Bhuvaraghan, B., Srinivasan, S.M., 2021. Dislocation density based crystal plasticity model incorporating the effect of precipitates in IN718 under monotonic and cyclic deformation. Int. J. Plast. 141, 102990 https://doi.org/10.1016/j.ijplas.2021.102990.

ALSHITS, V.I., 1992. The phonon-dislocation interaction and its rôle in dislocation dragging and thermal resistivity. pp. 625–697. https://doi.org/10.1016/B978-0-444-88773-3.50018-2.

Alshits, V.I., Darinskaya, E.V., Urusovskaya, A.A., 1985. The investigation of the shock deformation kinetics and dislocation dynamics upon pulse loading of CsI, NaCl, and LiF crystals. Physica Status Solidi 91, 533–542. https://doi.org/10.1002/pssa.2210910221 (a).

- Al'shitz, V.A., Indenbom, V.L., 1975. Dynamic dragging of dislocations. Soviet Phys. Uspekhi 18, 1–20. https://doi.org/10.1070/PU1975v018n01ABEH004689. Armstrong, R.W., Arnold, W., Zerilli, F.J., 2009. Dislocation mechanics of copper and iron in high rate deformation tests. J. Appl. Phys. 105 https://doi.org/10.1063/
- Austin, R.A., McDowell, D.L., 2012. Parameterization of a rate-dependent model of shock-induced plasticity for copper, nickel, and aluminum. Int. J. Plast. 32–33, 134-154. https://doi.org/10.1016/i.iiplas.2011.11.002.
- Austin, R.A., McDowell, D.L., 2011. A dislocation-based constitutive model for viscoplastic deformation of fcc metals at very high strain rates. Int. J. Plast. 27, 1-24. https://doi.org/10.1016/j.ijplas.2010.03.002.
- Babu, B., Lindgren, L.E., 2013. Dislocation density based model for plastic deformation and globularization of Ti-6Al-4V. Int. J. Plast. 50, 94-108. https://doi.org/ 10.1016/j.ijplas.2013.04.003.
- Baig, M., Khan, A.S., Choi, S.-H., Jeong, A., 2013. Shear and multiaxial responses of oxygen free high conductivity (OFHC) copper over wide range of strain-rates and temperatures and constitutive modeling. Int. J. Plast. 40, 65-80. https://doi.org/10.1016/j.ijplas.2012.07.004.
- Baik, S.C., Estrin, Y., Kim, H.S., Hellmig, R.J., 2003. Dislocation density-based modeling of deformation behavior of aluminium under equal channel angular pressing. Mater. Sci. Eng.: A 351, 86-97. https://doi.org/10.1016/S0921-5093(02)00847-X.
- Bao, H., Xu, H., Li, Y., Bai, H., Ma, F., 2022. The interaction mechanisms between dislocations and nano-precipitates in CuFe alloys: a molecular dynamic simulation. Int. J. Plast. 155 https://doi.org/10.1016/j.ijplas.2022.103317
- Barton, N.R., Bernier, J.V., Becker, R., Arsenlis, A., Cavallo, R., Marian, J., Rhee, M., Park, H.-S., Remington, B.A., Olson, R.T., 2011. A multiscale strength model for extreme loading conditions. J. Appl. Phys. 109 https://doi.org/10.1063/1.3553718.
- Bitzek, E., Gumbsch, P., 2004. Atomistic study of drag, surface and inertial effects on edge dislocations in face-centered cubic metals. Mater. Sci. Eng.: A 387-389, 11-15. https://doi.org/10.1016/j.msea.2004.01.092.
- Blaschke, D.N., 2019. Velocity dependent dislocation drag from phonon wind and crystal geometry. J. Phys. Chem. Solids 124, 24-35. https://doi.org/10.1016/j. jpcs.2018.08.032.
- Blaschke, D.N., Burakovsky, L., Preston, D.L., 2021. On the temperature and density dependence of dislocation drag from phonon wind. J. Appl. Phys. 130 https://doi. org/10.1063/5.0054536.
- Blaschke, D.N., Hunter, A., Preston, D.L., 2020. Analytic model of the remobilization of pinned glide dislocations: including dislocation drag from phonon wind. Int. J. Plast. 131, 102750 https://doi.org/10.1016/j.ijplas.2020.102750
- Bouaziz, O., Guelton, N., 2001. Modelling of TWIP effect on work-hardening. Mater. Sci. Eng. A 319-321, 246-249. https://doi.org/10.1016/S0921-5093(00)02019-
- Bryukhanov, I.A., 2020. Dynamics of edge dislocation in Cu-Ni solid solution alloys at atomic scale. Int. J. Plast. 135, 102834 https://doi.org/10.1016/j. iiplas,2020,102834.
- Cai, J., Griesbach, C., Ahnen, S.G., Thevamaran, R., 2023. Dynamic hardness evolution in metals from impact induced gradient dislocation density. Acta Mater. 249, 118807 https://doi.org/10.1016/j.actamat.2023.118807
- Cai, J., Thevamaran, R., 2020. Superior energy dissipation by ultrathin Semicrystalline polymer films under supersonic microprojectile impacts. Nano Lett. 20. 5632-5638, https://doi.org/10.1021/acs.nanolett.0c00066
- Cao, C.M., Tong, W., Bukhari, S.H., Xu, J., Hao, Y.X., Gu, P., Hao, H., Peng, L.M., 2019. Dynamic tensile deformation and microstructural evolution of AlxCrMnFeCoNi high-entropy alloys. Mater. Sci. Eng. A 759, 648-654. https://doi.org/10.1016/j.msea.2019.05.0
- Chandra, S., Samal, M.K., Chavan, V.M., Raghunathan, S., 2018. Hierarchical multiscale modeling of plasticity in copper: from single crystals to polycrystalline aggregates. Int. J. Plast. 101, 188-212. https://doi.org/10.1016/j.ijplas.2017.10.014.
- Chen, Q., Alizadeh, A., Xie, W., Wang, X., Champagne, V., Gouldstone, A., Lee, J.-H., Müftü, S., 2018. High-strain-rate material behavior and adiabatic material instability in impact of micron-scale Al-6061 particles. J. Therm. Spray Technol. 27, 641-653. https://doi.org/10.1007/s11666-018-0712-4.
- Chen, Q., Xie, W., Champagne, V.K., Nardi, A., Lee, J.-H., Müftü, S., 2023. On adiabatic shear instability in impacts of micron-scale Al-6061 particles with sapphire and Al-6061 substrates. Int. J. Plast. 166, 103630 https://doi.org/10.1016/j.ijplas.2023.103630.
- Clifton, R.J., 1985. Stress wave experiments in plasticity. Int. J. Plast. 1, 289-302. https://doi.org/10.1016/0749-6419(85)90016-6.
- Curtze, S., Kuokkala, V.T., 2010. Dependence of tensile deformation behavior of TWIP steels on stacking fault energy, temperature and strain rate. Acta Mater. 58, 5129–5141. https://doi.org/10.1016/j.actamat.2010.05.049.
- Dean, J., Clyne, T.W., 2017. Extraction of plasticity parameters from a single test using a spherical indenter and FEM modelling. Mech. Mater. 105, 112–122. https:// doi.org/10.1016/j.mechmat.2016.11.014
- Dharan, C.K.H., Hauser, F.E., 1973. High-velocity dislocation damping in aluminum. J. Appl. Phys. 44, 1468–1474. https://doi.org/10.1063/1.1662395.
- Dowding, I., Hassani, M., Sun, Y., Veysset, D., Nelson, K.A., Schuh, C.A., 2020. Particle size effects in metallic microparticle impact-bonding. Acta Mater. 194, 40–48. https://doi.org/10.1016/j.actamat.2020.04.044.
- Dubey, R., Jayaganthan, R., Ruan, D., Gupta, N.K., Jones, N., Velmurugan, R., 2023. Energy absorption and dynamic behaviour of 6xxx series aluminium alloys: a review. Int. J. Impact Eng. 172, 104397 https://doi.org/10.1016/j.ijimpeng.2022.104397
- El Ters, P., Shehadeh, M.A., 2019. Modeling the temperature and high strain rate sensitivity in BCC iron: atomistically informed multiscale dislocation dynamics simulations. Int. J. Plast. 112, 257-277. https://doi.org/10.1016/j.ijplas.2018.09.002.
- Elizalde, S., Ezequiel, M., Figueroa, I.A., Cabrera, J.M., Braham, C., Gonzalez, G., 2020. Microstructural evolution and mechanical behavior of an Al-6061 alloy processed by repetitive corrugation and straightening. Metals (Basel) 10, 489. https://doi.org/10.3390/met10040489.
- Estrin, Y., 1998. Dislocation theory based constitutive modelling: foundations and applications. J. Mater. Process. Technol. 80-81, 33-39. https://doi.org/10.1016/ S0924-0136(98)00208-8
- Estrin, Y., 1996. Dislocation-density-related constitutive modeling. In: Krausz, A.S., Krausz, K. (Eds.), Unified Constitutive Laws of Plastic Deformation. Elsevier, San Diego, pp. 69-106. https://doi.org/10.1016/B978-012425970-6/50003-5.
- Estrin, Y., Mecking, H., 1984. A unified phenomenological description of work hardening and creep based on one-parameter models. Acta Metallurgica 32, 57-70. https://doi.org/10.1016/0001-6160(84)90202-5
- Ferguson, W.G., Kumar, A., Dorn, J.E., 1967. Dislocation damping in aluminum at high strain rates. J. Appl. Phys. 38, 1863-1869. https://doi.org/10.1063/
- Follansbee, P.S., Kocks, U.F., 1988. A constitutive description of the deformation of copper based on the use of the mechanical threshold stress as an internal state variable. Acta Metallurgica 36, 81-93. https://doi.org/10.1016/0001-6160(88)90030-2.
- Frutschy, K.J., Clifton, R.J., 1998. High-temperature pressure-shear plate impact experiments on ofhc copper. J. Mech. Phys. Solids 46, 1723–1744. https://doi.org/ 10.1016/S0022-5096(98)00055-6
- Gao, C.Y., Zhang, L.C., 2012. Constitutive modelling of plasticity of fcc metals under extremely high strain rates. Int. J. Plast. 32–33, 121–133. https://doi.org/ 10.1016/j.ijplas.2011.12.001.
- Gasca-Neri, R., Nix, W.D., 1974. A model for the mobile dislocation density. Acta Metallurgica 22, 257-264. https://doi.org/10.1016/0001-6160(74)90165-5. Gilat, A., Clifton, R.J., 1985. Pressure-shear waves in 6061-T6 aluminum and alpha-titanium. J. Mech. Phys. Solids 33, 263-284. https://doi.org/10.1016/0022-5096 (85)90015-8.
- Gilman, J.J., 1969. Micromechanics of Flow in Solids. McGraw-Hill.
- $Gilman, J.J., 1965.\ Microdynamics\ of\ plastic\ flow\ at\ constant\ stress.\ J.\ Appl.\ Phys.\ 36,\ 2772-2777.\ https://doi.org/10.1063/1.1714577.$
- Gorman, J.A., Wood, D.S., Vreeland, T., 1969. Mobility of dislocations in aluminum at 74° and 83°K. J. Appl. Phys. 40, 903-904. https://doi.org/10.1063/1.1657491. Gourdin, W.H., Lassila, D.H., 1992. The mechanical behavior of pre-shocked copper at strain rates of 10-3-104s-1 and temperatures of 25-400°C. Mater. Sci. Eng. A 151, 11-18. https://doi.org/10.1016/0921-5093(92)90176-2.
- Granato, A.V., 1971. Dislocation inertial effects in the plasticity of superconductors. Phys. Rev. B 4, 2196–2201. https://doi.org/10.1103/PhysRevB.4.2196.
- Greenman, W.F., Vreeland, T., Wood, D.S., 1967. Dislocation mobility in copper. J. Appl. Phys. 38, 3595–3603. https://doi.org/10.1063/1.1710178.

- Griesbach, C., Cai, J., Jeon, S.-J., Thevamaran, R., 2023. Orientation-dependent plasticity mechanisms control synergistic property improvement in dynamically deformed metals. Int. J. Plast. 166, 103657 https://doi.org/10.1016/j.ijplas.2023.103657.
- Habib, S.A., Meredith, C.S., Khan, A.S., 2021. Quasi-static and dynamic investigation of an advanced high strength and corrosion resistant 10% Cr nanocomposite martensitic steel. Int. J. Mech. Sci. 211, 106774 https://doi.org/10.1016/j.ijmecsci.2021.106774.
- Haridas, R.S., Agrawal, P., Thapliyal, S., Yadav, S., Mishra, R.S., McWilliams, B.A., Cho, K.C., 2021. Strain rate sensitive microstructural evolution in a TRIP assisted high entropy alloy: experiments, microstructure and modeling. Mech. Mater. 156, 103798 https://doi.org/10.1016/j.mechmat.2021.103798.
- Harold, J.F., Ashby, M.F., 1982. Deformation of Mechanism Maps, The Plasticity and Creep of Metals and Ceramics, Pergamon Press.
- Hassani, M., Champagne, V.K., Helfritch, D., 2023. Bonding mechanisms in cold spray. Advances in Cold Spray. Elsevier, pp. 149–163. https://doi.org/10.1016/B978-0-08-103015-8.00004-9.
- Hassani, M., Veysset, D., Nelson, K.A., Schuh, C.A., 2020a. Material hardness at strain rates beyond 106 s-1 via high velocity microparticle impact indentation. Scr. Mater. 177, 198–202. https://doi.org/10.1016/j.scriptamat.2019.10.032.
- Hassani, M., Veysset, D., Sun, Y., Nelson, K.A., Schuh, C.A., 2020b. Microparticle impact-bonding modes for mismatched metals: from co-deformation to splatting and penetration. Acta Mater. 199, 480–494. https://doi.org/10.1016/j.actamat.2020.08.038.
- Hassani-Gangaraj, M., Veysset, D., Champagne, V.K., Nelson, K.A., Schuh, C.A., 2018a. Adiabatic shear instability is not necessary for adhesion in cold spray. Acta Mater. 158, 430–439. https://doi.org/10.1016/j.actamat.2018.07.065.
- Hassani-Gangaraj, M., Veysset, D., Nelson, K.A., Schuh, C.A., 2019. Impact-bonding with aluminum, silver, and gold microparticles: toward understanding the role of native oxide layer. Appl. Surf. Sci. 476, 528–532. https://doi.org/10.1016/j.apsusc.2019.01.111.
- Hassani-Gangaraj, M., Veysset, D., Nelson, K.A., Schuh, C.A., 2018b. In-situ observations of single micro-particle impact bonding. Scr. Mater. 145, 9–13. https://doi.org/10.1016/j.scriptamat.2017.09.042.
- Hassani-Gangaraj, M., Veysset, D., Nelson, K.A., Schuh, C.A., 2018c. Melt-driven erosion in microparticle impact. Nat. Commun. 9, 5077. https://doi.org/10.1038/s41467-018-07509-y.
- Hassani-Gangaraj, M., Veysset, D., Nelson, K.A., Schuh, C.A., 2017. Melting can hinder impact-induced adhesion. Phys. Rev. Lett. 119, 175701 https://doi.org/10.1103/PhysRevLett.119.175701.
- Hikata, A., Johnson, R.A., Elbaum, C., 1970. Interaction of dislocations with electrons and with phonons. Phys. Rev. B 2, 4856–4863. https://doi.org/10.1103/PhysRevB.2.4856.
- Hu, Q., Zhao, F., Fu, H., Li, K., Liu, F., 2017. Dislocation density and mechanical threshold stress in OFHC copper subjected to SHPB loading and plate impact. Mater. Sci. Eng. A 695, 230–238. https://doi.org/10.1016/j.msea.2017.03.112.
- Hunter, A., Preston, D.L., 2022. Analytic model of dislocation density evolution in fcc polycrystals accounting for dislocation generation, storage, and dynamic recovery mechanisms. Int. J. Plast. 151 https://doi.org/10.1016/j.ijplas.2021.103178.
- Hyon, J., Lawal, O., Fried, O., Thevamaran, R., Yazdi, S., Zhou, M., Veysset, D., Kooi, S.E., Jiao, Y., Hsiao, M.S., Streit, J., Vaia, R.A., Thomas, E.L., 2018. Extreme energy absorption in glassy polymer thin films by supersonic micro-projectile impact. Materials Today 21, 817–824. https://doi.org/10.1016/j.mattod.2018.07.014.
- Indenbom, V.L., Chernov, V.M., 1992. Thermally activated glide of a dislocation in a point defect field. pp. 517–570. https://doi.org/10.1016/B978-0-444-88773-3. 50016-9.
- $Jassby, K.M., Vreeland, T., 1973. \ Dislocation \ mobility \ in \ pure \ copper \ at \ 4.2\ ^{\circ}K. \ Phys. \ Rev. \ B \ 8, 3537-3541. \ https://doi.org/10.1103/PhysRevB.8.3537.$
- Jassby, K.M., Vreeland, T., 1971. Dislocation mobility in copper and zinc at 44°K. Scripta Metallurgica 5, 1007–1011. https://doi.org/10.1016/0036-9748(71)90146-3.
- Jassby, K.M., Vreeland, T., 1970. An experimental study of the mobility of edge dislocations in pure copper single crystals. Philos. Mag. 21, 1147–1168. https://doi.org/10.1080/14786437008238500.
- Jeong, K., Lee, H., Kwon, O.M., Jung, J., Kwon, D., Han, H.N., 2020. Prediction of uniaxial tensile flow using finite element-based indentation and optimized artificial neural networks. Mater. Des. 196 https://doi.org/10.1016/j.matdes.2020.109104.
- Jeong, K., Lee, K., Lee, S., Kang, S.-G., Jung, J., Lee, H., Kwak, N., Kwon, D., Han, H.N., 2022. Deep learning-based indentation plastometry in anisotropic materials. Int. J. Plast. 157, 103403 https://doi.org/10.1016/j.ijplas.2022.103403.
- Johnson, G.R., Cook, W.H., 1985. Fracture characteristics of three metals subjected to various strains, strain rates, temperatures and pressures. Eng. Fract. Mech. 21, 31–48. https://doi.org/10.1016/0013-7944(85)90052-9.
- Johnston, W.G., Gilman, J.J., 1959. Dislocation velocities, dislocation densities, and plastic flow in lithium fluoride crystals. J. Appl. Phys. 30, 129–144. https://doi.org/10.1063/1.1735121.
- Jun, T.-S., Armstrong, D.E.J., Britton, T.B., 2016. A nanoindentation investigation of local strain rate sensitivity in dual-phase Ti alloys. J. Alloys Compd. 672, 282–291. https://doi.org/10.1016/j.jallcom.2016.02.146.
- Khan, A.S., Kazmi, R., Farrokh, B., 2007. Multiaxial and non-proportional loading responses, anisotropy and modeling of Ti-6Al-4V titanium alloy over wide ranges of strain rates and temperatures. Int. J. Plast. 23, 931–950. https://doi.org/10.1016/j.ijplas.2006.08.006.
- Khan, A.S., Liang, R., 1999. Behaviors of three BCC metal over a wide range of strain rates and temperatures: experiments and modeling. Int. J. Plast. 15, 1089–1109. https://doi.org/10.1016/S0749-6419(99)00030-3.
- Khan, A.S., Sung Suh, Y., Kazmi, R., 2004. Quasi-static and dynamic loading responses and constitutive modeling of titanium alloys. Int. J. Plast. 20, 2233–2248. https://doi.org/10.1016/j.ijplas.2003.06.005.
- Kim, S., Kim, S.Y., 2021. Sudden transition of dislocation dynamics in FCC crystals at ultralow temperatures. Int. J. Plast. 140, 102979 https://doi.org/10.1016/j.ijplas.2021.102979.
- Klopp, R.W., Clifton, R.J., Shawki, T.G., 1985. Pressure-shear impact and the dynamic viscoplastic response of metals. Mech. Mater. 4, 375–385. https://doi.org/10.1016/0167-6636(85)90033-X.
- Kocks, U.F., Mecking, H., 2003. Physics and phenomenology of strain hardening: the FCC case. Prog. Mater Sci. 48, 171–273. https://doi.org/10.1016/S0079-6425 (02)00003-8.
- Ku, A.Y., Khan, A.S., Gnäupel-Herold, T., 2020. Quasi-static and dynamic response, and texture evolution of two overaged Al 7056 alloy plates in T761 and T721 tempers: experiments and modeling. Int. J. Plast. 130, 102679 https://doi.org/10.1016/j.ijplas.2020.102679.
- Kuksin, A.Yu., Stegailov, V.V., Yanilkin, A.V., 2008. Molecular-dynamics simulation of edge-dislocation dynamics in aluminum. Doklady Phys. 53, 287–291. https://doi.org/10.1134/S1028335808060013.
- Kuksin, A.Yu., Yanilkin, A.V., 2013. Atomistic simulation of the motion of dislocations in metals under phonon drag conditions. Phys. Solid State 55, 1010–1019. https://doi.org/10.1134/S1063783413050193.
- Kumar, A., Hauser, F.E., Dorn, J.E., 1968. Viscous drag on dislocations in aluminum at high strain rates. Acta Metallurgica 16, 1189–1197. https://doi.org/10.1016/0001-6160(68)90054-0.
- Kumar, A., Kumble, R.G., 1969. Viscous drag on dislocations at high strain rates in copper. J. Appl. Phys. 40, 3475–3480. https://doi.org/10.1063/1.1658222.
- Kumar, N., Ying, Q., Nie, X., Mishra, R.S., Tang, Z., Liaw, P.K., Brennan, R.E., Doherty, K.J., Cho, K.C., 2015. High strain-rate compressive deformation behavior of the Al0.1CrFeCoNi high entropy alloy. Mater. Des. 86, 598–602. https://doi.org/10.1016/j.matdes.2015.07.161.
- Landau, P., Shneck, R.Z., Makov, G., Venkert, A., 2009. Evolution of dislocation patterns in fcc metals. IOP Conf. Ser. Mater. Sci. Eng. 3, 012004 https://doi.org/10.1088/1757-899X/3/1/012004.
- Larkin, K., Hunter, A., Buechler, M., 2022. Simulation of dislocation evolution in microparticle impacts over a wide range of impact velocities. Int. J. Plast. 158, 103408 https://doi.org/10.1016/j.ijplas.2022.103408.
- Lee, J.-H., Loya, P.E., Lou, J., Thomas, E.L., 2014. Dynamic mechanical behavior of multilayer graphene via supersonic projectile penetration. Science 346 (1979), 1092–1096. https://doi.org/10.1126/science.1258544.

- Lee, J.-H., Veysset, D., Singer, J.P., Retsch, M., Saini, G., Pezeril, T., Nelson, K.A., Thomas, E.L., 2012. High strain rate deformation of layered nanocomposites. Nat. Commun. 3, 1164. https://doi.org/10.1038/ncomms2166.
- Lee, S., Barthelat, F., Hutchinson, J.W., Espinosa, H.D., 2006. Dynamic failure of metallic pyramidal truss core materials Experiments and modeling. Int. J. Plast. 22, 2118–2145. https://doi.org/10.1016/j.ijplas.2006.02.006.
- Lemiale, V., Estrin, Y., Kim, H.S., O'Donnell, R., 2010. Grain refinement under high strain rate impact: a numerical approach. Comput. Mater. Sci. 48, 124–132. https://doi.org/10.1016/j.commatsci.2009.12.018.
- Lennon, A.M., Ramesh, K.T., 2004. The influence of crystal structure on the dynamic behavior of materials at high temperatures. Int. J. Plast. 20, 269–290. https://doi.org/10.1016/S0749-6419(03)00037-8.
- Li, W.-Y., Zhang, C., Li, C.-J., Liao, H., 2009. Modeling aspects of high velocity impact of particles in cold spraying by explicit finite element analysis. J. Therm. Spray Technol. 18, 921–933. https://doi.org/10.1007/s11666-009-9325-2.
- Li, Y.Z., Huang, M.X., 2021. A dislocation-based flow rule with succinct power-law form suitable for crystal plasticity finite element simulations. Int. J. Plast. 138, 102921 https://doi.org/10.1016/j.ijplas.2020.102921.
- Li, Z., Voisin, T., McKeown, J.T., Ye, J., Braun, T., Kamath, C., King, W.E., Wang, Y.M., 2019. Tensile properties, strain rate sensitivity, and activation volume of additively manufactured 316L stainless steels. Int. J. Plast. 120, 395–410. https://doi.org/10.1016/j.ijplas.2019.05.009.
- Lichtenfeld, J.A., Van Tyne, C.J., Mataya, M.C., 2006. Effect of strain rate on stress-strain behavior of alloy 309 and 304L austenitic stainless steel. Metallur. Mater. Trans. A 37, 147–161. https://doi.org/10.1007/s11661-006-0160-5.
- Lieou, C.K.C., Mourad, H.M., Bronkhorst, C.A., 2019. Strain localization and dynamic recrystallization in polycrystalline metals: thermodynamic theory and simulation framework. Int. J. Plast. 119, 171–187. https://doi.org/10.1016/j.ijplas.2019.03.005.
- Liu, R., Salahshoor, M., Melkote, S.N., Marusich, T., 2015a. A unified material model including dislocation drag and its application to simulation of orthogonal cutting of OFHC Copper. J. Mater. Process. Technol. 216, 328–338. https://doi.org/10.1016/j.jmatprotec.2014.09.021.
- Liu, R., Salahshoor, M., Melkote, S.N., Marusich, T., 2014. A unified internal state variable material model for inelastic deformation and microstructure evolution in SS304. Mater. Sci. Eng. A 594, 352–363. https://doi.org/10.1016/j.msea.2013.11.071.
- Liu, R., Zhang, Z.J., Li, L.L., An, X.H., Zhang, Z.F., 2015b. Microscopic mechanisms contributing to the synchronous improvement of strength and plasticity (SISP) for TWIP copper alloys. Sci. Rep. 5, 9550. https://doi.org/10.1038/srep09550.
- Liu, W., Lian, J., Aravas, N., Münstermann, S., 2020. A strategy for synthetic microstructure generation and crystal plasticity parameter calibration of fine-grain-structured dual-phase steel. Int. J. Plast. 126, 102614 https://doi.org/10.1016/j.ijplas.2019.10.002.
- Liu, X., Wu, Y., Wang, Y., Chen, J., Bai, R., Gao, L., Xu, Z., Wang, W.Y., Tan, C., Hui, X., 2022. Enhanced dynamic deformability and strengthening effect via twinning and microbanding in high density NiCoFeCrMoW high-entropy alloys. J. Mater. Sci. Technol. 127, 164–176. https://doi.org/10.1016/j.jmst.2022.02.055.
- Lu, L., Dao, M., Kumar, P., Ramamurty, U., Karniadakis, G.E., Suresh, S., 2020. Extraction of mechanical properties of materials through deep learning from instrumented indentation. Proc. Natl. Acad. Sci. 117, 7052–7062. https://doi.org/10.1073/pnas.1922210117.
- Magagnosc, D.J., Lloyd, J.T., Meredith, C.S., Pilchak, A.L., Schuster, B.E., 2021. Incipient dynamic recrystallization and adiabatic shear bands in Ti–7Al studied via in situ X-ray diffraction. Int. J. Plast. 141, 102992 https://doi.org/10.1016/j.iiplas.2021.102992.
- Maier, V., Durst, K., Mueller, J., Backes, B., Höppel, H.W., Göken, M., 2011. Nanoindentation strain-rate jump tests for determining the local strain-rate sensitivity in nanocrystalline Ni and ultrafine-grained Al. J. Mater. Res. 26, 1421–1430. https://doi.org/10.1557/jmr.2011.156.
- Mayer, A.E., Lekanov, M.V., Grachyova, N.A., Fomin, E.V., 2022. Machine-learning-based model of elastic—plastic deformation of copper for application to shock wave problem. Metals (Basel) 12, 402. https://doi.org/10.3390/MET12030402/S1.
- Mecking, H., Kocks, U.F., 1981. Kinetics of flow and strain-hardening. Acta Metallurgica 29, 1865–1875. https://doi.org/10.1016/0001-6160(81)90112-7.
- Melanie, M., 1996. An introduction to genetic algorithms. Comput. Math. Appl. 32, 133. https://doi.org/10.1016/S0898-1221(96)90227-8.
- Meyers, M.A., 1994. Dynamic Behavior of Materials. Wiley. https://doi.org/10.1002/9780470172278.
- Meyers, M.A., Murr, L.E. (Eds.), 1981. Shock Waves and High-Strain-Rate Phenomena in Metals. Springer US, Boston, MA. https://doi.org/10.1007/978-1-4613-3219-0.
- Meyers, M.A., Vöhringer, O., Lubarda, V.A., 2001. The onset of twinning in metals: a constitutive description. Acta Mater. 49, 4025–4039. https://doi.org/10.1016/S1359-6454(01)00300-7.
- Moćko, W., Rodríguez-Martínez, J.A., Kowalewski, Z.L., Rusinek, A., 2012. Compressive viscoplastic response of 6082-T6 and 7075-T6 aluminium alloys under wide range of strain rate at room temperature: experiments and modelling. Strain 48, 498–509. https://doi.org/10.1111/j.1475-1305.2012.00847.x.
- Mohan, S., Millan-Espitia, N., Yao, M., Steenberge, N.V., Kalidindi, S.R., 2021. Critical evaluation of spherical indentation stress-strain protocols for the estimation of the yield strengths of steels. Exp. Mech. 61, 641–652. https://doi.org/10.1007/S11340-021-00689-7/FIGURES/5.
- Moon, J., Bouaziz, O., Kim, H.S., Estrin, Y., 2021. Twinning engineering of high-entropy alloys: an exercise in process optimization and modeling. Mater. Sci. Eng. A 822. https://doi.org/10.1016/j.msea.2021.141681.
- Mordehai, D., Ashkenazy, Y., Kelson, I., Makov, G., 2003. Dynamic properties of screw dislocations in Cu: A molecular dynamics study. Phys. Rev. B 67, 024112. https://doi.org/10.1103/PhysRevB.67.024112.
- Morrow, B.M., Lebensohn, R.A., Trujillo, C.P., Martinez, D.T., Addessio, F.L., Bronkhorst, C.A., Lookman, T., Cerreta, E.K., 2016. Characterization and modeling of mechanical behavior of single crystal titanium deformed by split-Hopkinson pressure bar. Int. J. Plast. 82, 225–240. https://doi.org/10.1016/j.ijplas.2016.03.006.
- Murr, L.E., 1988. Shock waves in condensed matter. In: Schmidt, S.C., Holmes, N.C. (Eds.), Shock Waves in Condensed Matter–1987: Proceedings of the American Physical Society Topical Conference. Elsevier, p. 315.
- Nadgornyi, E., 1988. Dislocation dynamics and mechanical properties of crystals. Prog. Mater Sci. 31, 1-530. https://doi.org/10.1016/0079-6425(88)90005-9.
- Nemat-Nasser, S., Guo, W., 2000. Flow stress of commercially pure niobium over a broad range of temperatures and strain rates. Mater. Sci. Eng. A 284, 202–210. https://doi.org/10.1016/S0921-5093(00)00740-1.
- Nemat-Nasser, S., Guo, W.G., Cheng, J.Y., 1999. Mechanical properties and deformation mechanisms of a commercially pure titanium. Acta Mater. 47, 3705–3720. https://doi.org/10.1016/S1359-6454(99)00203-7.
- Nemat-Nasser, S., Isaacs, J.B., 1997. Direct measurement of isothermal flow stress of metals at elevated temperatures and high strain rates with application to Ta and TaW alloys. Acta Mater. 45, 907–919. https://doi.org/10.1016/S1359-6454(96)00243-1.
- Nemat-Nasser, S., Li, Y., 1998. Flow stress of F.C.C. polycrystals with application to OFHC Cu. Acta Mater. 46, 565–577. https://doi.org/10.1016/S1359-6454(97)
- Nguyen, T., Luscher, D.J., Wilkerson, J.W., 2017. A dislocation-based crystal plasticity framework for dynamic ductile failure of single crystals. J. Mech. Phys. Solids 108, 1–29. https://doi.org/10.1016/j.jmps.2017.07.020.
- Nie, J., Li, S., Zhong, H., Hu, C., Lin, X., Chen, J., Guan, R., 2020a. Microstructure and mechanical properties of laser welded 6061-T6 aluminum alloy under high strain rates. Metals (Basel) 10, 1145. https://doi.org/10.3390/met10091145.
- Nie, Y., Claus, B., Gao, J., Zhai, X., Kedir, N., Chu, J., Sun, T., Fezzaa, K., Chen, W.W., 2020b. In Situ observation of adiabatic shear band formation in aluminum alloys. Exp. Mech. 60, 153–163. https://doi.org/10.1007/s11340-019-00544-w.
- Nieto-Fuentes, J.C., Rittel, D., Osovski, S., 2018. On a dislocation-based constitutive model and dynamic thermomechanical considerations. Int. J. Plast. 108, 55–69. https://doi.org/10.1016/j.ijplas.2018.04.012.
- Olmsted, D.L., HectorJr, L.G., Curtin, W.A., Clifton, R.J., 2005. Atomistic simulations of dislocation mobility in Al, Ni and Al/Mg alloys. Model. Simul. Mat. Sci. Eng. 13, 371–388. https://doi.org/10.1088/0965-0393/13/3/007.
- Oren, E., Yahel, E., Makov, G., 2017. Dislocation kinematics: a molecular dynamics study in Cu. Model Simul. Mat. Sci. Eng. 25, 025002 https://doi.org/10.1088/1361-651X/aa52a7.
- Osetsky, Y.N., Pharr, G.M., Morris, J.R., 2019. Two modes of screw dislocation glide in fcc single-phase concentrated alloys. Acta Mater. 164, 741–748. https://doi.org/10.1016/j.actamat.2018.11.020.

- Parameswaran, V.R., Urabe, N., Weertman, J., 1972. Dislocation mobility in aluminum. J. Appl. Phys. 43, 2982-2986. https://doi.org/10.1063/1.1661644.
- Park, J.M., Moon, J., Bae, J.W., Jang, M.J., Park, J., Lee, S., Kim, H.S., 2018. Strain rate effects of dynamic compressive deformation on mechanical properties and microstructure of CoCrFeMnNi high-entropy alloy. Mater. Sci. Eng. A 719, 155–163. https://doi.org/10.1016/j.msea.2018.02.031.
- Park, S., Marimuthu, K.P., Han, G., Lee, H., 2023. Deep learning based nanoindentation method for evaluating mechanical properties of polymers. Int. J. Mech. Sci. 246. 108162 https://doi.org/10.1016/j.ijmecsci.2023.108162.
- Patel, D.K., Kalidindi, S.R., 2017. Estimating the slip resistance from spherical nanoindentation and orientation measurements in polycrystalline samples of cubic metals. Int. J. Plast. 92, 19–30. https://doi.org/10.1016/j.ijplas.2017.03.004.
- Pogorelko, V.V., Mayer, A.E., 2023. Dynamic tensile fracture of iron: molecular dynamics simulations and micromechanical model based on dislocation plasticity. Int. J. Plast. 167, 103678 https://doi.org/10.1016/j.ijplas.2023.103678.
- Preston, D.L., Tonks, D.L., Wallace, D.C., 2003. Model of plastic deformation for extreme loading conditions. J. Appl. Phys. 93, 211–220. https://doi.org/10.1063/1.1524706.
- Queyreau, S., Marian, J., Gilbert, M.R., Wirth, B.D., 2011. Edge dislocation mobilities in bcc Fe obtained by molecular dynamics. Phys. Rev. B 84, 064106. https://doi.org/10.1103/PhysRevB.84.064106.
- Rahmati, S., Jodoin, B., 2020. Physically based finite element modeling method to predict metallic bonding in cold spray. J. Therm. Spray Technol. 29, 611–629. https://doi.org/10.1007/s11666-020-01000-1.
- Rahmati, S., Veiga, R.G.A., Zúñiga, A., Jodoin, B., 2021. A numerical approach to study the oxide layer effect on adhesion in cold spray. J. Therm. Spray Technol. 30, 1777–1791. https://doi.org/10.1007/s11666-021-01245-4.
- Regazzoni, G., Kocks, U.F., Follansbee, P.S., 1987. Dislocation kinetics at high strain rates. Acta Metallurgica 35, 2865–2875. https://doi.org/10.1016/0001-6160(87) 90285-9.
- Rhee, M., Zbib, H.M., Hirth, J.P., Huang, H., Rubia, T.de la, 1998. Models for long-/short-range interactions and cross slip in 3D dislocation simulation of BCC single crystals. Model. Simul. Mat. Sci. Eng. 6, 467–492. https://doi.org/10.1088/0965-0393/6/4/012.
- Rittel, D., Kidane, A.A., Alkhader, M., Venkert, A., Landau, P., Ravichandran, G., 2012. On the dynamically stored energy of cold work in pure single crystal and polycrystalline copper. Acta Mater. 60, 3719–3728. https://doi.org/10.1016/j.actamat.2012.03.029.
- Rittel, D., Zhang, L.H., Osovski, S., 2017. The dependence of the Taylor–Quinney coefficient on the dynamic loading mode. J. Mech. Phys. Solids 107, 96–114. https://doi.org/10.1016/j.jmps.2017.06.016.
- Rohatgi, A., Vecchio, K.S., Gray, G.T., 2001. The influence of stacking fault energy on the mechanical behavior of Cu and Cu-Al alloys: deformation twinning, work hardening, and dynamic recovery. Metallur. Material. Trans. A 32, 135–145. https://doi.org/10.1007/s11661-001-0109-7.
- Sakino, K., 2006. Strain rate dependence of dynamic flow stress considering viscous drag for 6061 aluminium alloy at high strain rates. J. de Physique IV (Proceedings) 134, 183–189. https://doi.org/10.1051/jp4:2006134028.
- Saleh, M., Xu, A., Hurt, C., Ionescu, M., Daniels, J., Munroe, P., Edwards, L., Bhattacharyya, D., 2019. Oblique cross-section nanoindentation for determining the hardness change in ion-irradiated steel. Int. J. Plast. 112, 242–256. https://doi.org/10.1016/j.ijplas.2018.08.015.
- Salehi, S.-D., Kingstedt, O., 2023. Critical assessment and demonstration of high-emissivity coatings for improved infrared signal quality for Taylor–Quinney coefficient experimentation. Int. J. Impact Eng. 178, 104593 https://doi.org/10.1016/j.ijimpeng.2023.104593.
- Schwarz, R.B., Isaac, R.D., Granato, A.V., 1977. Dislocation inertial effects in the plastic deformation of dilute alloys of lead and copper. Phys. Rev. Lett. 38, 554–557. https://doi.org/10.1103/PhysRevLett.38.554.
- Schwarz, R.B., Labusch, R., 1978. Dynamic simulation of solution hardening. J. Appl. Phys. 49, 5174-5187. https://doi.org/10.1063/1.324413.
- Soares, G.C., Hokka, M., 2021. The Taylor–Quinney coefficients and strain hardening of commercially pure titanium, iron, copper, and tin in high rate compression. Int. J. Impact Eng. 156, 103940 https://doi.org/10.1016/j.ijimpeng.2021.103940.
- Suzuki, T., Ikushima, A., Aoki, M., 1964. Acoustic attenuation studies of the frictional force on a fast moving dislocation. Acta Metallurgica 12, 1231–1240. https://doi.org/10.1016/0001-6160(64)90107-5.
- Systemes, Dassault, 2019. ABAQUS 2019 Documentation. Abaqus 2019.
- Thevamaran, R., Griesbach, C., Yazdi, S., Ponga, M., Alimadadi, H., Lawal, O., Jeon, S.-J., Thomas, E.L., 2020. Dynamic martensitic phase transformation in single-crystal silver microcubes. Acta Mater. 182, 131–143. https://doi.org/10.1016/j.actamat.2019.10.006.
- Thevamaran, R., Lawal, O., Yazdi, S., Jeon, S.-J., Lee, J.-H., Thomas, E.L., 2016. Dynamic creation and evolution of gradient nanostructure in single-crystal metallic microcubes. Science 354 (1979), 312–316. https://doi.org/10.1126/science.aag1768.
- Tiamiyu, A.A., Lucas, T., Pang, E.L., Chen, X., LeBeau, J.M., Schuh, C.A., 2023. Heterogeneous microstructural evolution during hydrodynamic penetration of a high-velocity copper microparticle impacting copper. Mater. Today. https://doi.org/10.1016/j.mattod.2023.11.015.
- Tian, Y., Chen, F., Cui, Z., Tian, X., 2023. Effects of atomic size misfit on dislocation mobility in FCC dense solid solution: atomic simulations and phenomenological modeling. Int. J. Plast. 160, 103504 https://doi.org/10.1016/j.ijplas.2022.103504.
- Toth, L.S., Molinari, A., Estrin, Y., 2002. Strain hardening at large strains as predicted by dislocation based Polycrystal plasticity model. J. Eng. Mater. Technol. 124, 71–77. https://doi.org/10.1115/1.1421350.
- Tong, W., Clifton, R.J., Huang, S., 1992. Pressure-shear impact investigation of strain rate history effects in oxygen-free high-conductivity copper. J. Mech. Phys. Solids 40, 1251–1294. https://doi.org/10.1016/0022-5096(92)90015-T.
- Varam, S., Rajulapati, K.V., Bhanu Sankara Rao, K., 2014. Strain rate sensitivity studies on bulk nanocrystalline aluminium by nanoindentation. J. Alloys Compd. 585, 795–799. https://doi.org/10.1016/j.jallcom.2013.09.116.
- Varshni, Y.P., 1970. Temperature dependence of the elastic constants. Phys. Rev. B 2, 3952-3958. https://doi.org/10.1103/PhysRevB.2.3952.
- Voisin, T., Grapes, M.D., Li, T.T., Santala, M.K., Zhang, Y., Ligda, J.P., Lorenzo, N.J., Schuster, B.E., Campbell, G.H., Weihs, T.P., 2020. In situ TEM observations of high-strain-rate deformation and fracture in pure copper. Mater. Today 33, 10–16. https://doi.org/10.1016/j.mattod.2019.11.001.
- Voisin, T., Grapes, M.D., Zhang, Y., Lorenzo, N.J., Ligda, J.P., Schuster, B.E., Santala, M.K., Li, T., Campbell, G.H., Weihs, T.P., 2017. DTEM In Situ mechanical testing: defects motion at high strain rates. In: Conference Proceedings of the Society for Experimental Mechanics Series. Springer New York LLC, pp. 209–213. https://doi.org/10.1007/978-3-319-41132-3 29.
- Vreeland, T., 1984. Dislocation drag in close-packed metals. Scripta Metallurgica 18, 645-651. https://doi.org/10.1016/0036-9748(84)90313-2.
- Wallace, D.C., 1981. Irreversible thermodynamics of overdriven shocks in solids. Phys. Rev. B 24, 5597-5606. https://doi.org/10.1103/PhysRevB.24.5597.
- Wang, B., Wang, C., Liu, B., Zhang, X., 2019a. Dynamic mechanical properties and microstructure of an (Al0.5CoCrFeNi)0.95Mo0.025C0.025 high entropy alloy. Entropy 21, 1154. https://doi.org/10.3390/e21121154.
- Wang, H., Dhiman, A., Ostergaard, H.E., Zhang, Y., Siegmund, T., Kruzic, J.J., Tomar, V., 2019b. Nanoindentation based properties of Inconel 718 at elevated temperatures: a comparison of conventional versus additively manufactured samples. Int. J. Plast. 120, 380–394. https://doi.org/10.1016/j.ijplas.2019.04.018.Wang, X., Hassani, M., 2020. Ultra-high strain rate constitutive modeling of pure titanium using particle impact test. J. Appl. Mech. 87 https://doi.org/10.1115/1.4047290.
- Wang, Y.Z., Jiao, Z.M., Bian, G.B., Yang, H.J., He, H.W., Wang, Z.H., Liaw, P.K., Qiao, J.W., 2022. Dynamic tension and constitutive model in Fe40Mn20Cr20Ni20 high-entropy alloys with a heterogeneous structure. Mater. Sci. Eng. A 839, 142837. https://doi.org/10.1016/j.msea.2022.142837.
- Wulf, G.L., 1979. High strain rate compression of titanium and some titanium alloys. Int. J. Mech. Sci. 21, 713–718. https://doi.org/10.1016/0020-7403(79)90051-1. Xie, W., Alizadeh-Dehkharghani, A., Chen, Q., Champagne, V.K., Wang, X., Nardi, A.T., Kooi, S., Müftü, S., Lee, J.-H., 2017. Dynamics and extreme plasticity of metallic microparticles in supersonic collisions. Sci. Rep. 7, 5073. https://doi.org/10.1038/s41598-017-05104-7.
- Xue, S., Fan, Z., Lawal, O.B., Thevamaran, R., Li, Q., Liu, Y., Yu, K.Y., Wang, J., Thomas, E.L., Wang, H., Zhang, X., 2017. High-velocity projectile impact induced 9R phase in ultrafine-grained aluminium. Nat. Commun. 8, 1653. https://doi.org/10.1038/s41467-017-01729-4.
- Yang, F., Dong, L., Cai, L., Wang, L., Xie, Z., Fang, F., 2021. Effect of cold drawing strain on the microstructure, mechanical properties and electrical conductivity of low-oxygen copper wires. Mater. Sci. Eng. A 818, 141348. https://doi.org/10.1016/j.msea.2021.141348.

- Yanilkin, A.V., Krasnikov, V.S., Kuksin, A.Yu., Mayer, A.E., 2014. Dynamics and kinetics of dislocations in Al and Al–Cu alloy under dynamic loading. Int. J. Plast. 55, 94–107. https://doi.org/10.1016/j.ijplas.2013.09.008.
- Ye, C., Liu, G., Chen, K., Liu, J., Hu, J., Yu, Y., Mao, Y., Shen, Y., 2023. Unified crystal plasticity model for fcc metals: from quasistatic to shock loading. Phys. Rev. B 107, 024105. https://doi.org/10.1103/PhysRevB.107.024105.
- Yuan, K., Guo, W., Li, D., Li, P., Zhang, Y., Wang, P., 2021. Influence of heat treatments on plastic flow of laser deposited Inconel 718: testing and microstructural based constitutive modeling. Int. J. Plast. 136, 102865 https://doi.org/10.1016/j.ijplas.2020.102865.
- Zaera, R., Rodríguez-Martínez, J.A., Rittel, D., 2013. On the Taylor–Quinney coefficient in dynamically phase transforming materials. Application to 304 stainless steel. Int. J. Plast. 40, 185–201. https://doi.org/10.1016/j.ijplas.2012.08.003.
- Zaretsky, E.B., Efremenkov, I., Kalabukhov, S., Hayun, S., 2023. Impact response of nitinol over 300–473 K temperature range. J. Appl. Phys. 134 https://doi.org/10.1063/5.0177087.
- Zaretsky, E.B., Kanel, G.I., 2013. Response of copper to shock-wave loading at temperatures up to the melting point. J. Appl. Phys. 114 https://doi.org/10.1063/1.4819328.
- Zhang, M., Li, J., Tang, B., Kou, H., Fan, J., 2018. Mechanical characterization and strain-rate sensitivity measurement of Ti-7333 alloy based on nanoindentation and crystal plasticity modeling. Progr. Natural Sci.: Mater. Int. 28, 718–723. https://doi.org/10.1016/j.pnsc.2018.10.003.
- Zhang, T.W., Ma, S.G., Zhao, D., Wu, Y.C., Zhang, Y., Wang, Z.H., Qiao, J.W., 2020. Simultaneous enhancement of strength and ductility in a NiCoCrFe high-entropy alloy upon dynamic tension: micromechanism and constitutive modeling. Int. J. Plast. 124, 226–246. https://doi.org/10.1016/j.ijplas.2019.08.013.
- Zhang, Z., Khan, M., Picu, C.R., 2023. Mechanism-informed constitutive modeling of molecular crystal cyclotetramethylene tetranitramine (β-HMX). Int. J. Plast. 169, 103722 https://doi.org/10.1016/j.ijplas.2023.103722.
- Zolotorevsky, N.Y., Rybin, V.V., Matvienko, A.N., Ushanova, E.A., Philippov, S.A., 2019. Misorientation angle distribution of deformation-induced boundaries provided by their EBSD-based separation from original grain boundaries: case study of copper deformed by compression. Mater. Charact. 147, 184–192. https://doi.org/10.1016/j.matchar.2018.11.003.